Materials Today Bio 26 (2024) 101081

Contents lists available at ScienceDirect

Materials Today Bio

journal homepage: www.journals.elsevier.com/materials-today-bio

A natural hydrogel complex improves intervertebral disc degeneration by correcting fatty acid metabolism and inhibiting nucleus pulposus cell pyroptosis

Dong Wang [a,b,c,1], Liangping Zhang [a,1], Du He [a], Yujun Zhang [a], Lan Zhao [b], Zhimin Miao [b], Wei Cheng [a,b], Chengyue Zhu [a,b,c], Yinyan Shao [a], Guofen Ge [a], Hang Zhu [a], HongTing Jin [a,d,**], Wei Zhang [a,b,c,***], Hao Pan [a,b,c,*]

[a] Department of Orthopaedics, Hangzhou TCM Hospital Affiliated to Zhejiang Chinese Medical University (Hangzhou Hospital of Traditional Chinese Medicine), Hangzhou, 310000, Zhejiang Province, PR China
[b] Department of Orthopaedics, Hangzhou Dingqiao Hospital, Huanding Road NO 1630, Hangzhou, 310021, Zhejiang Province, PR China
[c] Institute of Orthopaedics and Traumatology, Hangzhou Traditional Chinese Medicine Hospital Affiliated to Zhejiang Chinese Medical University, Tiyuchang Road NO 453, Hangzhou, 310007, Zhejiang Province, PR China
[d] Institute of Orthopaedics and Traumatology, The First Affiliated Hospital of Zhejiang Chinese Medical University, Hangzhou, PR China

ARTICLE INFO

Keywords:
Intervertebral disc degeneration
Nucleus pulposus
Fibrinogen
Vesicles
Pyroptosis
Fatty acid metabolism

ABSTRACT

The degeneration of intervertebral discs is strongly associated with the occurrence of pyroptosis in nucleus pulposus (NP) cells. This pyroptosis is characterized by abnormal metabolism of fatty acids in the degenerative pathological state, which is further exacerbated by the inflammatory microenvironment and degradation of the extracellular matrix. In order to address this issue, we have developed a fibrin hydrogel complex (FG@PEV). This intricate formulation amalgamates the beneficial attributes of platelet extravasation vesicles, contributing to tissue repair and regeneration. Furthermore, this complex showcases exceptional stability, gradual-release capabilities, and a high degree of biocompatibility. In order to substantiate the biological significance of FG@PEV in intervertebral disc degeneration (IVDD), we conducted a comprehensive investigation into its potential mechanism of action through the integration of RNA-seq sequencing and metabolomics analysis. Furthermore, these findings were subsequently validated through experimentation in both in vivo and in vitro models. The experimental results revealed that the FG@PEV intervention possesses the capability to reshape the inflammatory microenvironment within the disc. It also addresses the irregularities in fatty acid metabolism of nucleus pulposus cells, consequently hindering cellular pyroptosis and slowing down disc degeneration through the regulation of extracellular matrix synthesis and degradation. As a result, this injectable gel system represents a promising and innovative therapeutic approach for mitigating disc degeneration.

1. Introduction

The incidence of spinal musculoskeletal disorders, specifically those associated with low back pain (LBP), has been steadily on the rise due to the aging of our society. This upward trend has imposed a substantial burden on both the healthcare system and the socioeconomic landscape, with LBP disorders now standing as a prominent cause of disability among patients [1–3]. Nonetheless, according to statistical data, a significant portion, ranging from 26 % to 42 %, of patients grappling with low back pain are afflicted by disc degeneration [4]. In the course of intervertebral disc degeneration, the NP tissue undergoes a depletion in direct blood supply, leading to a situation where the nucleus pulposus

* Corresponding author. Department of Orthopaedics, Hangzhou TCM Hospital Affiliated to Zhejiang Chinese Medical University Hangzhou 310000, Zhejiang Province, PR China
** Corresponding author. Institute of Orthopaedics and Traumatology, The First Affiliated Hospital of Zhejiang Chinese Medical University, Hangzhou, PR China
*** Corresponding author. Department of Orthopaedics, Hangzhou TCM Hospital Affiliated to Zhejiang Chinese Medical University Hangzhou, 310000, Zhejiang Province, PR China mail:
E-mail addresses: hongtingjin@163.com (H. Jin), volcano8060@163.com (W. Zhang), harper1966@alu.zcmu.edu.cn (H. Pan).
[1] These author contributed equally to this work.

https://doi.org/10.1016/j.mtbio.2024.101081
Received 14 February 2024; Received in revised form 26 March 2024; Accepted 2 May 2024
Available online 3 May 2024

cells (NPCs) find themselves in a hypoxic and nutrient-deprived microenvironment. This circumstance renders these cells extremely vulnerable to inflammatory agents and the accumulation of reactive oxygen species (ROS) [5]. Furthermore, the activation of inflammatory factors and reactive oxygen species can induce apoptosis in nucleus pulposus cells, thereby intensifying the progression of disc degeneration [6]. The worsening of disc degeneration initiates a subsequent cascade of anabolic and catabolic processes within the intervertebral disc, ultimately culminating in structural deterioration and biomechanical instability [7,8]. Ultimately, this process contributes to the development of low back pain and spinal sequence instability. Consequently, there is significant practical value in investigating the mechanism of nucleus pulposus cell death to prolong the treatment of intervertebral disc degeneration.

Cellular pyroptosis primarily represents an inflammatory variant of programmed cell death, relying on NLRP3 inflammatory vesicles to drive the advancement of persistent inflammatory responses and ensuing tissue deterioration [9]. Recent studies have unveiled that the activation of NLRP3 inflammatory vesicles triggers the synthesis of IL-1β and IL-18, consequently inducing metabolic disturbances and cellular damage within the nucleus pulposus. This phenomenon is intricately associated with the degeneration of intervertebral discs, commonly referred to as IVDD [10].

Moreover, research has elucidated that disturbances in lipid metabolism exert a substantial influence on cellular pyroptosis. For example, reduced levels of phospholipids and their oxidized derivatives, such as phosphatidylinositol 4-phosphate (PI4P), lead to decreased binding and oligomerization of GSDMD-N within cells. Conversely, the accumulation of PI4P fosters the activation of NLRP3 inflammasomes [11]. Fatty acid oxidation stands as the primary pathway for the breakdown and subsequent metabolism of fatty acids. In macrophages, fatty acid beta-oxidation (FAO) plays a pivotal role in generating ROS by engaging NADPH oxidase 4 (NOX4) and triggering the activation of NLRP3 inflammatory vesicles [12]. Hence, correcting disorders in fatty acid metabolism to inhibit pyroptosis in NPCs could potentially represent a promising therapeutic strategy for addressing intervertebral disc degeneration.

Platelet extracellular vesicles (PEVs) are released by activated platelets and typically have diameters spanning from approximately 80 to 600 nm. These vesicles wield both physiological and pathological regulatory influences, encompassing the modulation of immunity, inflammation, and cellular proliferation. Moreover, they hold the potential to stimulate cellular healing responses and augment regenerative capabilities [13–16]. Additionally, it has been noted that PEVs possess the capacity to facilitate intercellular communication by transporting biologically active molecules, including membrane receptors, proteins, lipids, and nucleic acids, to specific target cells [17]. Recent research has brought to light that platelet extracellular vesicles have the capacity to restore impaired mitochondrial function, reduce oxidative stress, and rejuvenate myeloid cell metabolism by regulating the sirtuin 1 (SIRT1)-PGC1α-mitochondrial transcription factor A (TFAM) pathway. As a result, this intervention effectively retards the progression of IVDD [18]. Moreover, research has indicated that PEVs endow mast cells with 12-lipoxygenase, thereby enabling the synthesis of lipotoxic A4, a potent anti-inflammatory agent. In light of the closed and avascular nature of intervertebral discs, intervertebral injections are deemed an optimal treatment approach for IVDD [19]. Nonetheless, relying solely on the administration of extracellular vesicles proves inadequate for achieving lasting effects due to their limited duration of efficacy [20]. The regular administration of injections presents patients with both psychological and financial challenges, leading to suboptimal treatment adherence and an elevated risk of complications [21]. Hence, the construction and development of carriers possessing slow-release capabilities hold significant importance. Fibrin, a biopolymer obtained from blood coagulation proteins, presents itself as an optimal carrier option due to its commendable biocompatibility and extensive utilization in degenerative ailments like bone and joint disorders [22–24]. Furthermore, fibrin gels have the potential to exert a significant impact by serving as scaffolding structures and exerting anti-inflammatory effects [25–27]. Hence, the objective of this current study is to develop an optimal hydrogel material that possesses the dual capabilities of promoting tissue regeneration and repair, while also inhibiting inflammation, in order to effectively mitigate the progression of intervertebral disc degeneration.

In this study, platelet-derived vesicles were crosslinked with fibrinogen using thrombin to fabricate a platelet vesicle fibrin hydrogel, denoted as FG@PEV. The resultant hydrogel displayed favorable stability, exhibited a controlled release effect, and demonstrated biocompatibility. Importantly, it effectively mitigated LPS-induced scorched death in nucleus pulposus cells. In a rat caudal disc degeneration model, FG@PEV demonstrated its capability to alleviate the degradation of the extracellular matrix (ECM) by suppressing the inflammatory microenvironment within the intervertebral disc. This innovative methodology holds significant promise as a novel approach to tackle intervertebral disc degeneration.

2. Material and methods

2.1. Preparation and characterization of isolated PEV

In this study, blood samples were collected from healthy donors, and the collection process was approved by Hangzhou Hospital of Traditional Chinese Medicine. All donors provided informed consent and signed an informed consent form. In the subsequent step, blood obtained from healthy donors was combined with an anticoagulant and then subjected to centrifugation at 100×*g* for 15 min. Following this, the supernatant was collected and subjected to a second centrifugation at 800×*g* for 20 min. The centrifuged precipitate was preserved at room temperature after resuspension for subsequent use. To produce PEVs, platelet concentrates (1×10^6 cells/mL) underwent a sequence of filtration steps to isolate PEVs. The pore size of the filters was sequentially reduced from 1000 nm to 500 nm using polycarbonate membrane filters (Whatman, MA, USA) in a small extruder (Avanti Polar Lipid, AL, USA), and then further reduced to 200 nm. This process was repeated six times. The PEVs were collected by centrifuging at 15,000 g for 30 min. PLTs and PEVs were scrutinized using a cryo-transmission electron microscope, while their particle size and zeta potential were quantified through dynamic light scattering (DLS). PLTs and PEVs were assessed for particle stability using DLS at 0, 1, 3, 5, and 7 days. To investigate the release profile of PEV, 2 mg FG@PEV was immersed in PBS and incubated at 37 ± 1 °C on a horizontal shaker at 60 rpm. At designated time intervals (0.5, 1, 2, 3, 4, 5, 6, 7, and 8 days), BCA protein assay kit was used to measure the concentration of exosomes in the supernatant collected with supplemented PBS. Additionally, PLTs and PEVs proteins were separated using a protein isolation kit (Invitrogen, Carlsbad, USA) and their concentrations were measured with a BCA kit (Beyotime, China). Protein expression levels of PLTs and PEVs were analyzed through SDS-PAGE. Distinctions in protein expression between PLTs and PEVs were assessed using Caulmers Brilliant Blue staining (Beyotime, China).

2.2. Preparation of FG@PEV

A combination of platelet extravasated vesicles and fibrinogen (2 mg/mL 0.5 mL) was introduced to thrombin protein (2 mg/mL 0.05 mL) in order to initiate the formation of FG@PEV gel-like gel. The rheological properties of the FG were assessed using a sophisticated rheological swelling system (TA Instruments, USA), and the viscosity of the hydrogel was analyzed through steady shear scanning. Dynamic frequency scan analysis was conducted to quantify the frequency-dependent storage (G′) and loss (G″) moduli of the gels. The porosity of the gel was examined using ImageJ software (NIH, Bethesda, MD) in conjunction with

transmission electron microscopy to observe its morphology. To assess the release profile of PEV, DiO labeling was employed prior to its combination with plasma, and the resulting mixture was obtained through thrombin activation. The release characteristics of PEV were evaluated by measuring the fluorescence intensity of DiO in PBS over a period of 72 h at a temperature of 37 °C.

2.3. Cell culture

Sprague-Dawley (SD) rats, aged one week, were procured from the Animal Experiment Center of Zhejiang University of Traditional Chinese Medicine, China. Nucleus pulposus cells were isolated from the nucleus pulposus tissue of the caudal intervertebral discs. Primary nucleus pulposus cells were obtained through a continuous digestion process using type II collagenase (Solarbio, China) for 4 h at 37 °C. The cells collected from the isolated nucleus pulposus tissue of the caudal intervertebral discs were filtered twice through a 40 μm filter and then subjected to centrifugation at 1000 rpm for 5 min. The obtained NPCs were subsequently cultured in complete Dulbecco's Modified Eagle's Medium (DMEM, Gibco, USA), supplemented with 10 % fetal bovine serum (FBS, Sigma-Aldrich, USA), and 1 % streptomycin-penicillin solution (Gibco, USA). This culture was maintained within a cell incubator with 5 % CO_2. The medium was refreshed every other day, and cell passaging was carried out once the cell density reached 80 %. The second passage of cells was employed for subsequent experiments.

2.4. Evaluation of materials for cytotoxicity and proliferation

Upon reaching a confluence of 70–80 % during sub-culturing, NPCs were seeded into 96-well plates at a density of 1×10^4 cells per well and incubated for 24 h. Subsequently, the cells were exposed to varying concentrations of PEV (0.05, 0.1, 0.15, 0.2, 0.25, and 0.3 mg/mL) for 24 h to assess their cytotoxic effects, employing the CCK-8 assay (APExBio, USA). Following this, the cells were treated with diverse concentrations of FG@PEV (0, 0.5, 1, 2, 3, and 4 mg/mL) for 24 h to evaluate their cytotoxicity using the CCK-8 assay. Based on the findings from the previous experiment, the optimal concentration of FG@PEV was determined to be 2 mg/mL. In the subsequent experiment, 2 mg/mL of FG@PEV was introduced to the NPCs, and the proliferative potential of the NPCs after incubation for 1, 3, 5, and 7 days was evaluated using the CCK-8 assay kit and Calcein-AM/PI Double Stain Kit (yeasen, China). Cell quantification was carried out by measuring the optical density (OD) at 450 nm using a microplate reader. The experimental procedures were replicated three times.

2.5. Cytokine detection

Cytokine levels of 0.2 mg/mL PLTs and 0.2 mg/mL PEVs were assessed in the presence or absence of thrombin, respectively. The concentrations of IL-1β and TNF-α were determined utilizing ELISA assays (BMS-224-2, BMS213-2, Thermo Fisher Scientific, USA). The entire experimental procedure was replicated three times.

2.6. ROS detection and evaluation

ROS levels in NPCs were gauged using Reactive Oxygen Species Assay Kit (Beyotime, China). NPCs were pre-exposed to the complate DMEM medium with 200 μM H_2O_2 for 6 h before the experiment. Then, the NPCs were categorized into five groups: control (Con), H_2O_2-treated (H_2O_2), H_2O_2 + PEV-treated (PEV), H_2O_2 + FG-treated (FG), and H_2O_2 + FG@PEV-treated (FG@PEV) groups. These groups were then incubated for another 24 h. Subsequently, intervertebral disc nucleus pulposus cells were incubated with a 20 mM 2′,7′-dichlorodihydrofluorescein diacetate (DCFH-DA, Beyotime, China) at 37 °C for 20 min. Afterward, the cells underwent three rinses with serum-free medium before proceeding to flow cytometry analysis (Beckman, USA). The fluorescence signal intensity was evaluated by quantifying the oxidative conversion of DCFH-DA. It is important to note that all experiments were conducted in quadruplicate.

2.7. Flow cytometry

The cells were subjected to pretreatment with chlorpromazine (50 μM), Filipin III (7.5 μM), wortmannin (5 μM), and cytochalasin D (5 μM) in accordance with the manufacturer's instructions for a duration of 0.5 h. Subsequently, the cells were incubated with FG@PEV with DiI labeling for 24 h at either 37 °C or 4 °C. Following this, the culture medium and unendocytosed FG@PEV were removed by washing the cells three times with PBS buffer. The percentage of DiI-positive cells in each cell group was determined using flow cytometry (FACS) equipment, based on the fluorescence signal of DiI.

2.8. Western blot

Total proteins were extracted from the NPCs using a RIPA buffer containing a 1 % PMSF (Beyotime, China). The protein concentration in each group of cells was quantified using BCA protein concentration kit (Beyotime, China). Proteins were separated using 10 % SDS-PAGE and transferred from the gel to a polyvinylidene fluoroether membrane (Millipore, China). The fluoroether membrane was blocked with 5 % non-fat milk for 1 h. After blocking, the membrane was washed with Tris-HCl-buffered saline (TBST) containing 0.1 % Tween-20 three times for 5 min each. Subsequently, the membranes were incubated with NLRP3,Caspase1, GSDMD, Col2α, SOX9, Aggrecan, MMP3, MMP13, Adamts5 and GAPDH at 4 °C for 12 h; the internal control was GAPDH. The membrane was incubated with a specific horseradish peroxidase-conjugated secondary antibody (Beyotime, China) for 1 h at 18–25 °C after washing with TBST three times for 5 min each. Excess secondary antibody was washed away with TBST three times for 5 min each. Finally, the signal intensity of the reactive bands on the membrane was visualized using the ChemiDoc Touch imaging system (Bio-Rad, USA). All above experiments were performed in triplicate.

2.9. Quantitative real-time polymerase chain reaction (qPCR) analysis

The cells were divided into five groups: control (Con), LPS + ATP treatment (LPS), LPS + ATP with PEV treatment (PEV), LPS + ATP with FG treatment (FG), and LPS + ATP with FG@PEV treatment (FG@PEV). Following cell treatment, total RNA was extracted from the NP tissue using TRIzol reagent (Aidlab, China). In parallel, total RNA was also isolated from cultured cells and subjected to reverse transcription in accordance with the manufacturer's instructions. For the reverse transcription process, 1 μg of RNA was employed, and the All-in-One First Strand cDNA Synthesis Kit (GeneCopoeia, USA) was used. Subsequently, the samples were amplified using the ABI7900 Eco Real-Time PCR System (Thermo Fisher Scientific, USA) with BeyoFast™ SYBR Green qPCR Mix (Beyotime, China). The results were normalized utilizing the GAPDH gene and the $2^{-\Delta\Delta Ct}$ method. Primer sequences for qRT-PCR are provided in Table S1.

2.10. Lactic acid detection

The cells were subsequently categorized into five distinct groups: control (Con), LPS + ATP (LPS), LPS + ATP + PEV (PEV), LPS + ATP + FG (FG), and LPS + ATP + FG@PEV (FG @PEV). After 24 or 48 h of stimulation, the content of lactic acid in the supernatant of different groups of cells was measured by the LDH Cytotoxicity Assay Kit (Beyotime, China). The absorbance at 530 nm in the LDH release assay was measured using a SpectraMax M2 fluorescence enzyme marker and analyzed with SoftMax Pro version 5 software (Molecular Devices) to assess the cellular metabolic status. The experiments were conducted in quadruplicate.

2.11. Evaluation of cellular uptake to study intracellular transport and endosomal escape

NPCs were seeded in confocal dishes at a density of 1×10^5 cells and cultured overnight. Following this, Cy5.5-labeled FG@PEV was introduced into the dishes at a concentration of 2 mg/mL. After an incubation period of 2 and 4 h, the cells were washed three times with PBS and then fixed with 4 % paraformaldehyde at 37 °C for 10 min. To stain the cell nuclei, 4′,6-Diamidino-2-Phenylindole (DAPI) was added to the dishes for 5 min. For the purpose of determining the intracellular localization of FG@PEV, lysosomes were stained using Lysotracker Green (ThermoFisher Scientific, USA). Subsequently, the NPCs were visualized using a confocal laser scanning microscope (CLSM, Leica Microsystems, LAS X 3.5.5.19976).

2.12. Establishment of rat IVDD model

The animal studies adhered to the ethical regulations and protocols approved by the Management Committee in the Animal Experiment Center of Zhejiang University of Traditional Chinese Medicine. In this study, the IVDD rat model was established using the fine-needle puncture method, and male sd rats (200–250 g, 8 weeks old) were randomly allocated into five groups. The IVDD model was induced by caudal interstitial needling [28]. Following disinfection with iodine, a 26G needle (with a diameter of 0.45 mm) syringe needle was palpably inserted at the fibrous ring level and traversed through the NP to reach the opposing fibrous ring. No mortality or morbidity was observed throughout the experimental procedure. Subsequent to the surgical intervention, the rats were relocated to a warm and ventilated setting to facilitate anesthesia recovery, provided with regular feeding post-surgery, and subsequently assessed at 4 and 8 weeks post-treatment.

2.13. Radiological assessment analysis

The rats were anesthetized at the fourth and eighth weeks after modeling, and their molded tails were cut off and put into paraformaldehyde for later use. At 4 and 8 weeks post-drug injection, micro-CT (SkyScan, Belgium) and MRI magnetic resonance (Universal Corporation, USA) were utilized to evaluate rat cohorts, aiming to detect changes in nucleus pulposus signal intensity and intervertebral interspace height. Micro-CT was employed for disc height measurement, from which the disc height index (DHI) was calculated, representing the average anterior, middle, and posterior disc height. Change in DHI was computed relative to the initial 0-week value. CT images were analyzed with Data-viewer software, using the formula: $DHI = 2 \times (A + B + C)/(D + E + F + G + H + I)$; DHI% = measured DHI/NC group DHI × 100 %. Meanwhile, ImageJ software was used to quantify T2-weighted signal intensity of the nucleus pulposus in each disc from MRI images. The evaluations were conducted by three experienced radiologists and three orthopedic surgeons. Based on the revised Thomson classification [29], the categorization of MRI images encompassed grades I to IV, where grade I indicated normal findings, grade II denoted a slight reduction in signal intensity accompanied by significant narrowing of the high-signal area, grade III indicated a moderate decrease in signal density, and grade IV represented a severe decrease in signal.

2.14. Histological analysis

At the 4th and 8th week following drug administration, euthanasia was performed on all rats using an excess of carbon dioxide. The respective intervertebral disc segments were extracted and the samples were temporarily preserved in a 4 % paraformaldehyde solution. Subsequently, the skin and muscle tissues were carefully peeled away, and the samples were subjected to decalcification by immersing them in a decalcification solution (14 % EDTA, pH = 7.2) for a duration of 4 weeks. Meanwhile, changing the decalcification solution once a week. Paraffin-embedded tissues were prepared. Histological sections with a thickness of 8 μm were prepared using a slicer. H&E staining and senna staining (Safranin-O) were conducted, and digital scanning microscopy was employed to capture photographs for the purpose of analyzing the nucleus pulposus of the intervertebral discs, as well as assessing fibrotic pathology and structural alterations. The observed disc changes were subsequently classified into five distinct categories, in accordance with the established histological grading criteria [30].

2.15. Immunofluorescence staining

Each group of NPCs was fixed with 4 % paraformaldehyde on Petri dishes for 20 min. Following this, cells underwent three PBS washes and were permeabilized with 0.5 % Triton X-100 (Sigma-Aldrich, USA) (diluted in PBS) for 20 min. Subsequently, NPCs were blocked with 5 % Bovine Serum Albumin (BSA) for 30 min. NLRP3 (1:100, Proteintech, China), GSDMD (1:100, Proteintech, China), Col2α (1:100; Proteintech, China), and MMP13 (1:100, Proteintech, China) were then incubated with NPCs for 12 h at 4 °C. Cells were subsequently subjected to fluorescent dye incubation. This was followed by incubation with a fluorescent secondary antibody (goat anti-rabbit Alexa Fluor 488, 1:500, Beyotime, China) for 1 h at room temperature, and then with DAPI for 10 min. Images were captured using a fluorescence confocal microscope (Nikon, Tokyo, Japan). These experiments were repeated a total of five times.

2.16. Immunohistochemistry

Rat caudal intervertebral discs were collected and fixed in 4 % paraformaldehyde for 48 h. The discs were then decalcified using ethylenediaminetetraacetic acid for a period of 14 days. Following decalcification, the discs were dehydrated, embedded in paraffin, and sectioned at a thickness of 4 μm. For immunohistochemical (IHC) staining, the sections were deparaffinized using xylene and rehydrated with ethanol. Antigen retrieval was performed using citrate buffer (0.1, pH 6.0). After blocking with peroxidase blocking solution and normal horse serum, the sections were incubated with the primary antibody overnight at 4 °C. Next, the sections were subjected to incubation with biotinylated IgG and streptavidin-horseradish peroxidase. Immunoreactivity was observed using the DAB Peroxidase Substrate Kit (Beyotime, China). Subsequently, the sections were restained with hematoxylin and sealed. In the case of IF staining, the sections were prepared following the same protocol as for IHC staining. After blocking with QuickBlock™ blocking buffer (Beyotime, China) supplemented with Triton 100, the sections were incubated with the primary antibody at 4 °C overnight. Subsequently, the sections were incubated with anti-mouse/rabbit Alexa Fluor 488 or 568 secondary antibodies. Finally, the tissues were processed accordingly.

2.17. Collection of specimens

Nucleus pulposus tissue was obtained from a cohort of 10 patients diagnosed with lumbar disc herniation who underwent discectomy at our institution. The collected specimens were promptly fixed in RNAlate solution and cryopreserved following tissue penetration. Magnetic resonance imaging (MRI) was utilized to classify the intervertebral discs based on the pfirrmann grading system, where grade I/II denoted non-degenerated discs and grade VI/V represented degenerated discs. The cohort consisted of 5 cases of degenerated discs and 5 cases of non-degenerated discs, comprising 6 males and 4 females, with ages ranging from 35 to 71 years.

2.18. Metabolite extraction, detection and analysis

The medium was aspirated from cultured cells using a pipette, with

approximately 5 × 10^7 cells per sample. Subsequently, the cells were washed with PBS at 37 °C and the PBS was subsequently removed. To solubilize the samples, 800 μL of cold methanol/acetonitrile (1:1, v/v) was added, followed by re-solubilization in 100 μL of acetonitrile/water (1:1, v/v) solvent. The samples were then subjected to analysis using LC-MS. The extracts were analyzed using quadrupole time-of-flight mass spectrometry (Sciex TripleTOF 6600) with electrospray ionization affinity chromatography, specifically for non-targeted metabolomics. The mass spectrometer was utilized in both negative and positive ion modes, and the data were subjected to analysis by converting the unprocessed mass spectrometry (MS) data (wiff. scan files) into MzXML files using ProteoWizard MSConvert. Subsequently, the converted data were imported into the XCMS software. The processed data underwent normalization and were then imported into SIMCA-P (version 14.1, Umetrics, Umea, Sweden). The identification of metabolite-enriched pathways was conducted by querying the Online Encyclopedia of Genomes (KEGG) database and subsequently mapping them to corresponding pathways within the KEGG database.

2.19. Transcriptome analysis

Transcriptome analysis was conducted to ascertain the RNA Integrity Number (RIN) value, utilizing Agilent Technologies, located in CA, USA. The purification of mRNA from 1 μg of total RNA was achieved through the utilization of oligo (dT) magnetic beads, followed by mRNA fragmentation in ABclonal First Strand Synthesis Reaction Buffer. Subsequently, the fragmented mRNA was further processed in the ABclonal First Strand Synthesis Reaction Buffer. The PCR product was purified, and the quality of the library was evaluated using an Agilent Bioanalyzer 4150. The sequencing procedure was conducted on the NovaSeq 6000 (or MGISEQ-T7) sequencing platform, utilizing PE150 read lengths. Data obtained from the Illumina (or BGI) platform were employed for bioinformatics analysis, with the reference genome mapping tool Hisat2 being selected. The DESeq2 R package was utilized to analyze differential expression between the two groups. Genes exhibiting adjusted p-values <0.05 as determined by DESeq2 were classified as differentially expressed genes (DEGs). The clusterProfiler R package was employed to perform GO, KEGG, and GSEA enrichment analyses on the differential genes, thereby elucidating the functional enrichment of the differences.

2.20. Statistical analysis

The descriptive data were presented as absolute numbers and percentages, or as means and standard deviations. To evaluate the significance of differences between the two treatment groups, two-sided tests of unpaired t-tests were employed. For the analysis of three or more groups of patients, one-way analysis of variance (ANOVA) was conducted, followed by Tukey's post hoc test to determine statistical significance between the groups. Statistical significance was defined as p-values< 0.05. The analyses were carried out using Excel and GraphPad Prism.

3. Results

3.1. Inflammation leads to NLRP3 activation to promote myeloid cell pyroptosis

NPCs were subjected to LPS + ATP stimulation for a duration of 24 h in order to induce an inflammatory milieu akin to that observed in simulated intervertebral disc degeneration. To assess the clustering or aberrant values of degenerative NPCs, a comparative analysis was conducted using RNA-seq on samples of LPS-stimulated NPCs and normal NPCs, both exposed to the stimulation for 24 h. The findings of this study indicate a robust activation of pro-inflammatory markers and inflammatory pathways in the NPCs when subjected to LPS + ATP stimulation (Fig. 1A and Fig. S1). Additionally, the PCA analysis revealed significant differences in the expression levels of mRNAs between LPS + ATP stimulated degenerative NPCs and normal NPCs (Fig. S2). The genes that met the criteria of logFC≥2 and p-value <0.05 were analyzed for enrichment in Gene Ontology (GO) and Kyoto Encyclopedia of Genes and Genomes (KEGG) using the DAVID database. The GO enrichment analysis revealed enrichment in molecular functions related to cytokine activity and receptor-ligand activity, while the biological processes were primarily associated with inflammatory response and other processes. Additionally, the cellular components were found to be enriched in the extracellular region part, among others (Fig. 1B). Furthermore, the outcomes of KEGG enrichment analysis revealed a widespread activation of inflammation-related pathways, including the NOD-like receptor signaling pathway, TNF signaling pathway, and Toll-like receptor signaling pathway, among others, in NPCs upon exposure to LPS (Fig. 1C). Conversely, GSEA enrichment analysis indicated a suppression of the reactive oxygen species metabolism process and fatty acid metabolism process in NPs cells (Fig. 1D and E). NLRP3 serves as a significant indicator of inflammation, as indicated by transcriptome data demonstrating heightened expression of NLRP3 in NPCs upon LPS + ATP stimulation (Fig. 1F). To further ascertain the impact of NLRP3 expression on intervertebral disc degeneration, immunohistochemical (IHC) validation was performed on rat IVDD model and human degenerated intervertebral disc specimens to assess NLRP3 expression (Fig. 1G–J). The immunohistochemistry (IHC) results revealed increased levels of inflammation marker, NLRP3, in degenerated intervertebral discs in comparison to normal discs. The activation of NLRP3 may lead to the activation of pyroptosis classical inflammasome, leading to pyroptosis of NPCs. These findings collectively indicate the activation of a widespread inflammatory state and an elevation in NLRP3 expression during the process of disc degeneration.

3.2. FG@PEV preparation and characterization

PEV was derived from PLT and activated through the addition of thrombin coagulation to PEV and fibrin, resulting in the formation of FG@PEV hydrogel. This hydrogel was subsequently administered via injection into the intervertebral discs of rats (Fig. 2A). The properties of PEV were investigated using cryotransmission electron microscopy, revealing a small size range of 100–120 nm (Fig. 2B). Moreover, DLS analysis determined particle sizes and zeta potentials of PEV and PLT. PEV displayed a particle size of 121.6 nm and a zeta potential of −4.5 mV (Fig. 2C). To explore the underlying cause of the observed phenomenon, the protein composition of platelets (PLTs) and platelet-derived extracellular vesicles (PEVs) was investigated. Notably, similarities in protein composition between PLTs and PEVs were evident in Thomas Brilliant Blue staining (Fig. 2D). Specifically, membrane marker proteins (CD9, CD41, and CD63) were significantly enriched in PEVs. The expression of the extracellular vesicle negative marker calnexin is decreased in PEVs, while cytoplasmic proteins (GAPDH and β-actin) in PLTs were comparatively lower in PEVs.This indicates that most membrane proteins are well preserved, while the differential components are mainly concentrated in some cytoplasmic proteins (Fig. 2E). Next, we compared the inflammatory cytokine production of PLTs and PEVs upon thrombin activation. Platelets showed a notable rise in IL-1β and TNF-α production after thrombin addition. Conversely, PEVs displayed no significant alteration in inflammatory factor levels before and after thrombin addition, unlike PLTs. Platelets typically release various factors, including coagulation factors, growth factors, adhesion molecules, and inflammatory factors, upon activation [31]. These proteins can be classified into two categories: stored proteins and synthesized proteins. Many platelet-secreted factors (such as transforming growth factor β, TGF-β) are stored in processed or precursor forms and can be rapidly released, while others (such as interleukin-1β) are products of a rapid synthesis pathway triggered by activation signals received by platelets themselves (signal-dependent translation process of mRNA) [32]. We found that PEVs obtained through physical squeezing did not

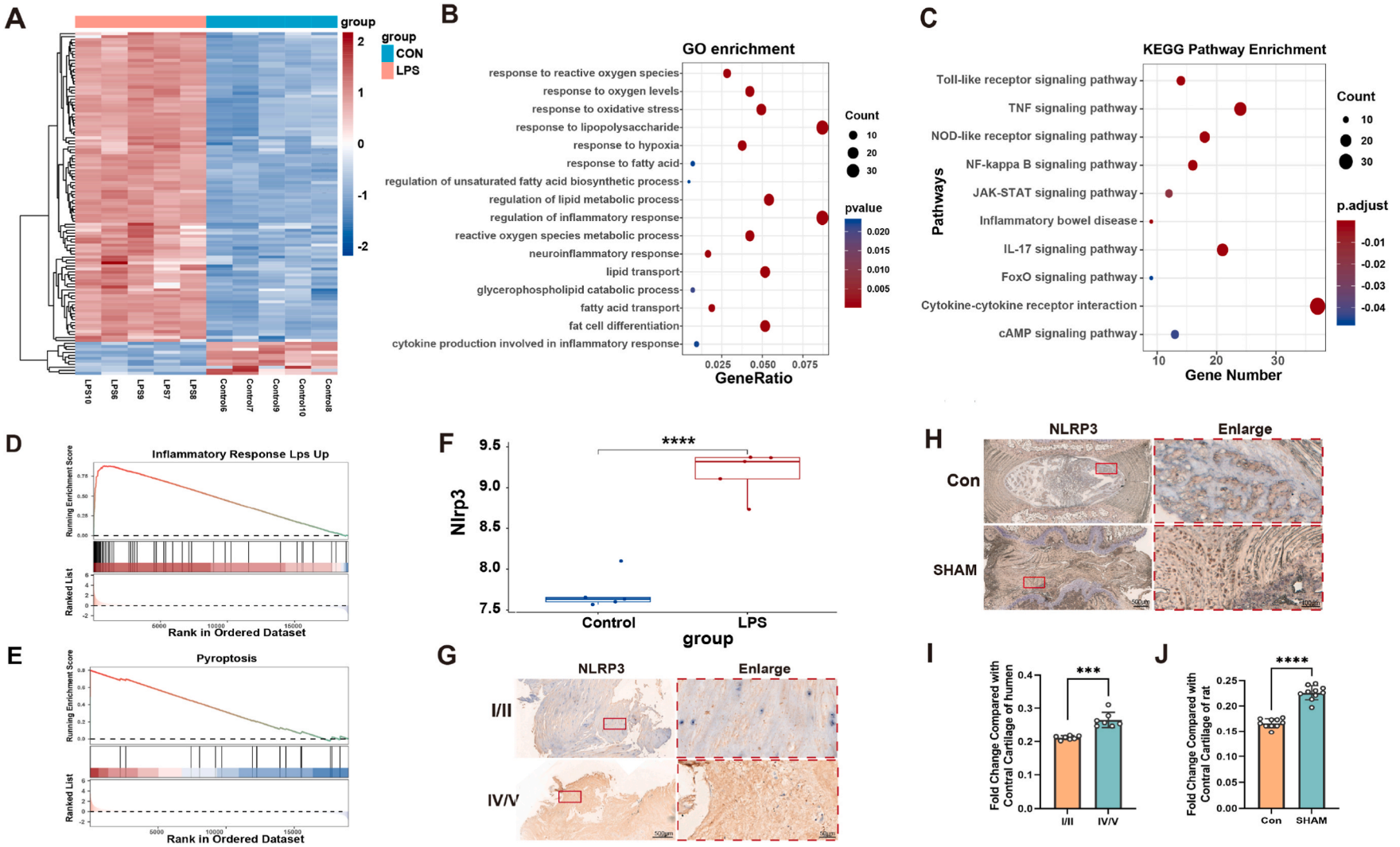

Fig. 1. Inflammation leads to NLRP3 activation promoting nucleus pulposus cell pyroptosis. (A) Heat map of genes differing in NPCs stimulated with LPS + ATP and normal cells. (n = 5) (B) Top 30 enriched gene ontology (GO) pathways for differential genes. (C) The first 20 enriched KEGG pathways. (D–E) Differential gene GSEA enrichment analysis. (F) Expression levels of NLRP3 in LPS + ATP stimulated and normal-treated nucleus pulposus cells. (G) Immunohistochemistry of NLRP3 in human intervertebral discs pfirrmann graded as grade I/II and VI/V. (H) Immunohistochemistry of NLRP3 in normal and degenerated rat intervertebral discs. (I) Quantitative analysis of NLRP3 immunohistochemical expression in human intervertebral discs. (J) Quantitative analysis of NLRP3 immunohistochemical expression in rat intervertebral discs. Data are expressed as mean ± SD (n = 5). (* : $P < 0.05$, ** : $P < 0.01$, *** : $P < 0.001$) .

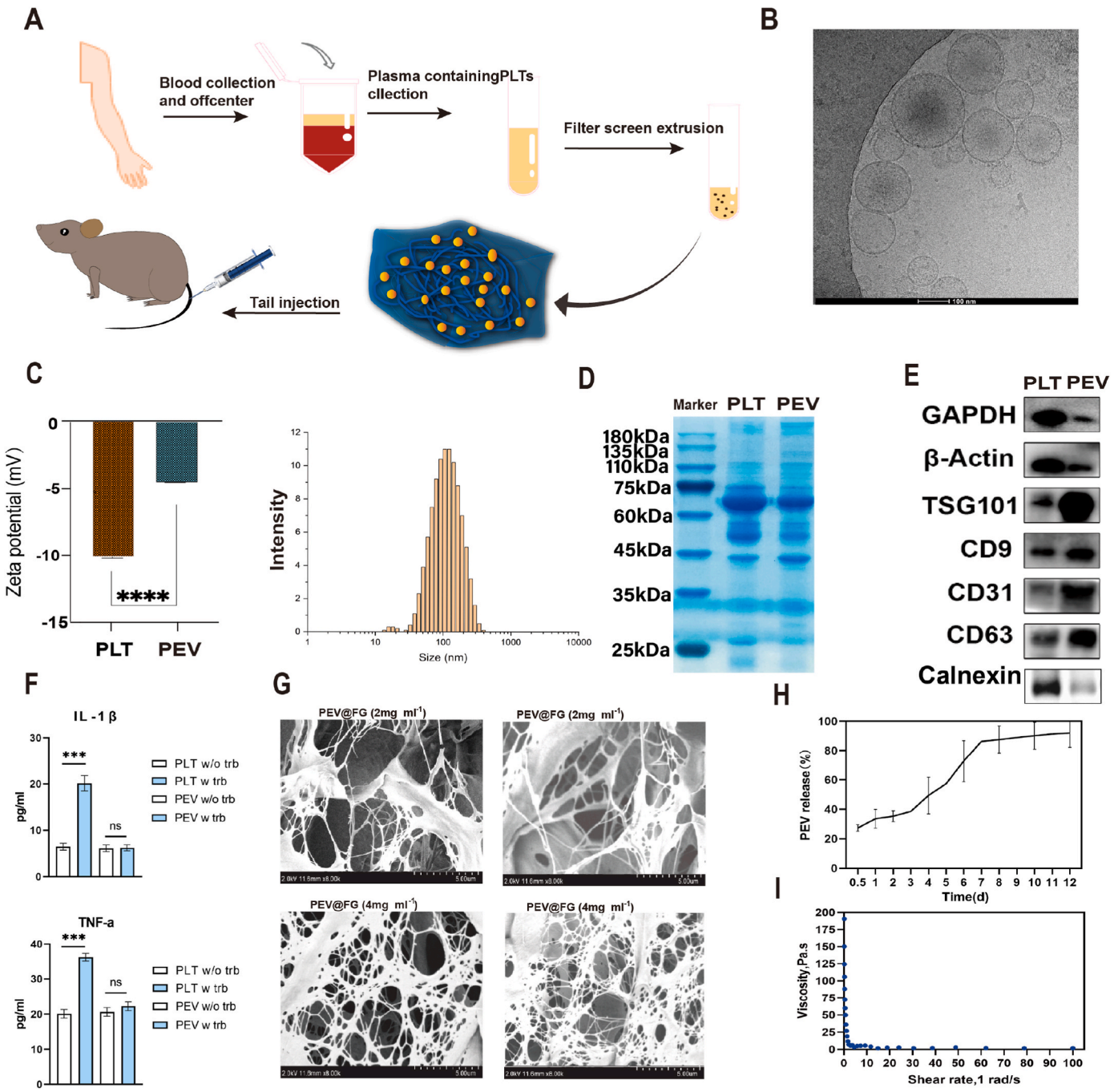

Fig. 2. Synthesis and characterization of FG@PEV. (A) Description and technical theory of in vitro preparation of PEV. (B) Cryo-transmission electron microscopy images of PEV. Scale bar = 100 nm. (C) Potential difference between PLT and PEV. Particle size of PEV. (D) SDS-PAGE of PLT and PEV, stained with Coomassie Brilliant Blue. (E) Protein blot analysis of CD41, TSG101, β-actin, GAPDH, CD63, CD9 and calnexin from PLT and PEV lysates. (F) Amounts of IL-1 and TNF-α cytokines from PLT and PEV in the presence and absence of thrombin. (G) Scanning electron microscopy (SEM) observations of NPV-ECM structures at different fibrinogen concentrations (2 and 4 mg mL-l); scale bar, 5 μm. (H) Control-release curves of FG@PEV. (I) Viscosity change of FG@PEV at shear rates from 1/s to 100/s. The significance between every two groups was calculated using a two-tailed Student's t-test or one-way analysis of variance (ANOVA) with Tukey's post-hoc test. Data are expressed as mean ± SD (n = 5) (* : $P < 0.05$, ** : $P < 0.01$, *** : $P < 0.001$) . (For interpretation of the references to colour in this figure legend, the reader is referred to the Web version of this article.)

significantly release inflammatory factors after thrombin activation, possibly because PEVs lose polysomes (particles larger than 50 nm in diameter containing two or more ribosomes), which may lead to an inability to receive activation signals to trigger the synthesis pathway. (Fig. 2F). Upon freeze-drying, the scanning electron microscopy (SEM) analysis revealed a smooth mesh 3D morphology in the FG@PEV microstructure (Fig. 2G). Furthermore, the gelatinous nature of FG@PEV, which is a combination of FG and PEV, was observed at room temperature, as depicted in Figure FG@PEV. Notably, FG@PEV exhibited a more consistent liquid stat (Fig. S1). The slow-release curve further substantiated the remarkable slow-release capability of FG@PEV, with a significant portion of FG@PEV being gradually released within a 12-day period (Fig. 2H). Moreover, as the shear rate increased gradually, the viscosity of FG@PEV exhibited a continuous decrease, indicating its shear-thinning property and favorable injection performance (Fig. 2I). Subsequently, the rheological properties of

FG@PEV were assessed in order to analyze its mechanical characteristics. Notably, FG@PEV exhibited considerably higher G″ values compared to G′ values, thereby signifying its state of low viscosity (Fig. S2).

3.3. Biocompatibility and lysosomal escape of FG@PEV

To confirm the endocytosis pathway of FG@PEV in NPCs, we subjected the cells to pretreatment with chlorpromazine, filipin III, wortmannin, and cytochalasin D for 0.5 h, followed by incubation with FG@PEV for 24 h at either 37 °C or 4 °C. The inhibitors effectively

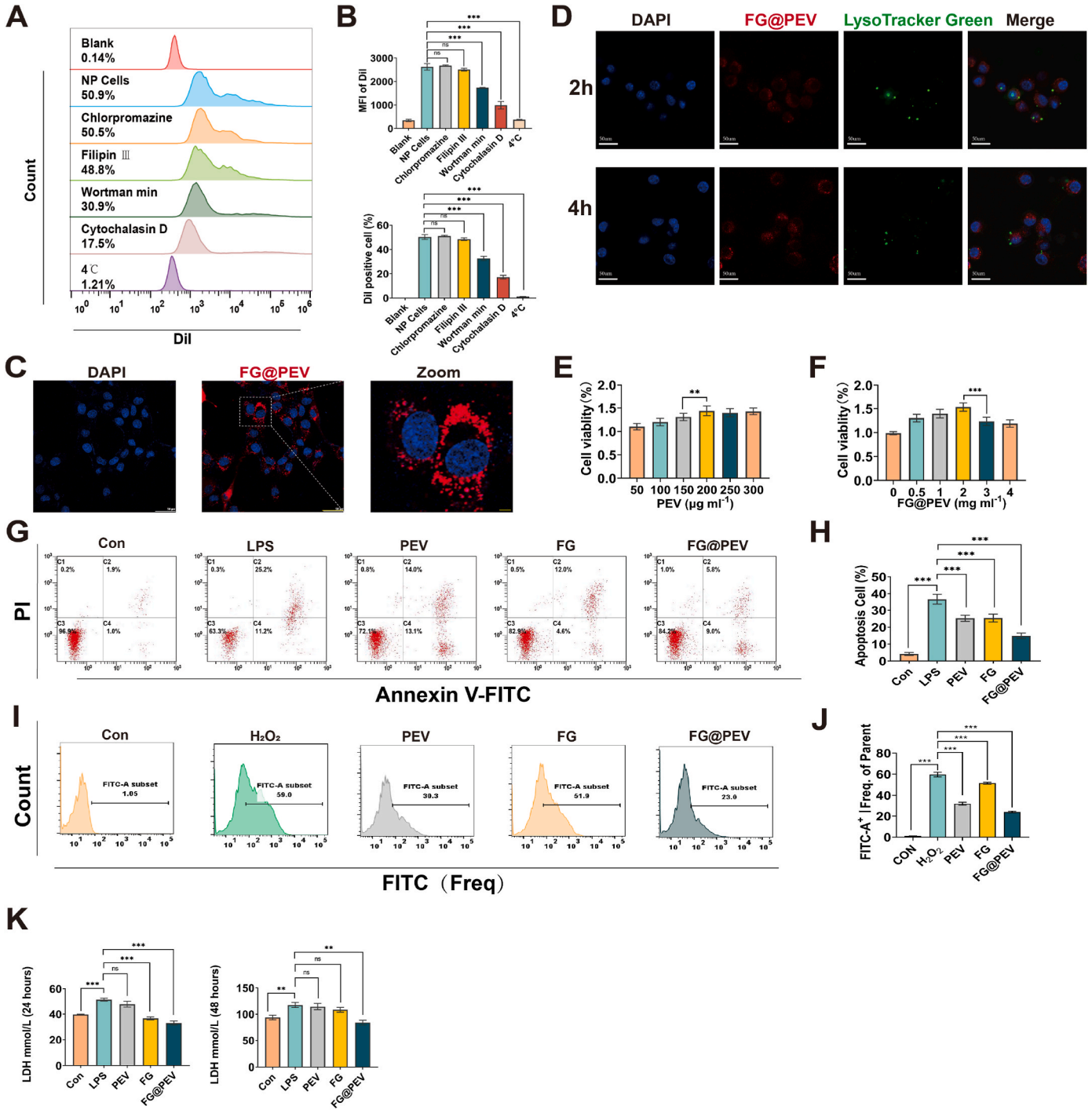

Fig. 3. Biocompatibility and lysosomal escape of FG@PEV. (A) NPCs measured by flow cytometry in the presence of each inhibitor (chlorpromazine, Filipin III, wortmannin, and cytochalasin D). (B) Flow cytometry-based quantification of specific immunofluorescence intensities (MFI) and the percentage of Dil-positive cells. (C) Fluorescence confocal microscopy images of FG@PEV uptake; scale bar, 50 μm. (D) Images of localization in NPCs under FG@PEV treatment at different times; scale bar, 50 μm; (E) Effect of different concentrations of PEV on NP cell activity as determined by CCK-8 kit. (F) Effect of different concentrations of FG@PEV on NP cell activity as determined by CCK-8 kit. (G) Detection of NPCs apoptosis by flow cytometry. (H) Quantitative analysis of NPCs apoptosis ratio in each group. (I) The ROS level was determined by flow cytometry with DCFH-DA probe. (J) The ROS abundance of NPCs according to (I). (K) Lactate content in the supernatant of LPS + ATP induced myeloid cell culture medium treated with FG, PEV, and FG@PEV, respectively. Data are expressed as mean ± SD (n = 5). (* : $P < 0.05$, ** : $P < 0.01$, *** : $P < 0.001$) .

hindered lattice protein-mediated endocytosis, cytosolic burrowing-type invagination-mediated endocytosis, microcellular endocytosis, and actin-mediated endocytosis, respectively. Flow cytometry analysis revealed NP cell positivity for DiI, with percentages of 0.14 %, 50.9 %, 50.5 %, 48.8 %, 30.9 %, 17.5 %, and 1.21 % in the control, chlorpromazine, filipin III, cytochalasin D, wortmannin, and 4 °C groups, respectively (Fig. 3A). These findings indicate that the uptake of FG@PEV by cells was hindered at 4 °C in the presence of cytochalasin D or wortmannin, but not affected by Filipin III or chlorpromazine (Fig. 3B). Hence, the cellular uptake of FG@PEV nanoparticles, measuring 100–120 nm in diameter, was facilitated through actin-mediated endocytosis in NPCs. Furthermore, a small fraction of FG@PEV nanoparticles were internalized by microcells due to their larger size. Subsequently, we employed a DiI membrane probe to label FG@PEV nanoparticles and incubated them with NPCs. Focusing microscopy revealed the endocytosis of FG@PEV nanoparticles by NPCs (Fig. 3C). The successful evasion of lysosomal degradation is crucial for the therapeutic effectiveness of FG@PEV nanoparticles. LysoTracker Green staining revealed the presence of green fluorescence in lysosomes, while a minor amount of red fluorescence was observed within the NPCs following a 2-h labeling period with Cy5.5-conjugated FG@PEV. The red fluorescence observed in NPCs incubated with FG@PEV indicated the internalization of a small quantity of FG@PEV by the cells. After a 4-h treatment, a reduction in the overlapping green and red fluorescence and an increase in red fluorescence were observed within the cells, suggesting the internalization of FG@PEV by the cells (Fig. 3D). The presence of FG@PEV in the cytoplasm suggests a successful detachment from the lysosome within the cells.

In order to investigate the impact of FG@PEV on NPCs, an examination of its activity and proliferative effects was conducted. Initially, NPCs were incubated with PEV, and the viability of the cells was monitored after a 24-h period. Subsequently, the toxicity of various concentrations of PEV on NPCs was assessed using the CCK-8 kit (Fig. 3E). Furthermore, NPCs were subjected to further incubation with FG@PEV, and the toxicity of different concentrations of FG@PEV on NPCs was determined using the CCK-8 kit (Fig. 3F). In accordance with the findings, a concentration of 2 mg/mL of FG@PEV was selected for further investigations. Subsequently, the impact of FG@PEV on the proliferation of NPCs was assessed using a CCK-8 kit. The cell proliferation assay involved monitoring the quantity of NPCs at 1, 3, and 5 days post FG@PEV treatment. The outcomes indicated a significant enhancement in proliferation facilitated by FG@PEV (Figs. S5–S6). Subsequently, We utilized the methods of FITC-annexin V/PI apoptosis assay to verify the effect of PEVs on the apoptosis. The percentages of NPCs apoptosis rates were determined to be 1.9 %, 25.2 %, 14.0 %, 12.0 %, and 5.8 % in the control, LPS, FG + LPS, PEV + LPS, and FG@PEV + LPS groups, respectively (Fig. 3G). The results indicate that FG@PEV has a significantly greater ability to reduce NP cell apoptosis (Fig. 3H). Further, we quantified H_2O_2-induced ROS production by flow cytometry. The percentages of DCF-positive NPCs were 1.05 %, 59.0 %, 30.3 %, 51.9 % and 23.0 in the control, H_2O_2, PEVs, FG and FG@PEV groups, respectively (Fig. 3I and J). Together, these results suggest that FG@PEV have a better antioxidant capacity than that of other groups. These findings suggest that FG@PEV exhibits a greater capacity for scavenging ROS and protecting the NPCs. It could reduce the proportion of apoptosis in NPCs (Fig. 3H). The content of lactic acid produced by LDH production in different groups of NPCs was further investigated after culturing NPCs in vitro for 24 h and 48 h under LPS + ATP stimulation. Lactate, a significant product of anaerobic glycolysis, exhibited an increase in response to LPS stimulation, indicating a decrease in the metabolizing capacity of reactive oxygen species. However, this effect was mitigated by the addition of FG@PEV (Fig. 3I).

3.4. Effect of FG@PEV on the inhibition of LPS + ATP stimulated inflammation and pyroptosis

Activation of NLRP3 and cleavage of GSDMD are often considered as markers of inflammation and pyroptosis, with elevated expression levels observed in degenerated discs. According to western blot results, protein expression levels of NLRP3, cleaved-caspase1, and GSDMD-N increased after stimulation with LPS and ATP, while protein expression levels of cells treated with FG@PEV decreased significantly (Fig. 4A). Immunofluorescence analysis demonstrated a decrease in fluorescence quantification of NLRP3 and GSDMD in cells treated with FG@PEV, in comparison to nucleus pulposus cells stimulated with LPS + ATP (Fig. 4B–D). Following this, we conducted a quantitative polymerase chain reaction (qPCR) analysis to further evaluate the alterations in cellular pyroptosis-related marker genes (ASC, NLRP3, IL-1β, and Caspase-1). The findings revealed a decrease in pro-inflammatory mRNA levels subsequent to the administration of FG@PEV treatment, indicating the inhibitory effect of FG@PEV on NPCs inflammation (Fig. 4E) and inhibited pyroptosis of NPCs by the classical inflammasome pathway. Moreover, the gene expression patterns in the three groups exhibited differential characteristics in principal component analysis (PCA), aligning with the results obtained from RNA-seq sequencing (Figs. S7–S8). In the LPS and FG@PEV groups, a total of 22,151 genes were identified, out of which 753 genes exhibited differential expression (|log2|fold change R1, $p < 0.05$) (Fig. 4F). Following high expression, FG@PEV demonstrated a mitigating effect on the inflammatory stimuli of GSDMD and NLRP3 in the LPS + ATP treatment (Fig. 4G). In order to investigate the subsequent pathway responses following FG@PEV administration, we conducted an analysis of the differentially expressed genes (DEGs) utilizing the clusterprofile package for KEGG pathway enrichment analysis. The outcomes revealed a significant emphasis on the TNF signaling pathway, NF-kappa B, MAPK signaling pathway, inflammation-related pathway, as well as pathways such as ECM-receptor interaction (Fig. 4H). Gene set enrichment analysis (GSEA) was employed to determine the impact of FG@PEV treatment on various cellular processes. Our findings indicate that the addition of FG@PEV treatment effectively enhances cellular reactive oxygen species metabolism, suppresses inflammatory responses, inhibits adipose synthesis, and promotes adipocyte differentiation processes when compared to the LPS group (Fig. 4I).

3.5. FG@PEV promotes free fatty acid metabolism after induction of cellular inflammation models

To gain a deeper understanding of the inhibitory effects of FG@PEV on inflammation and pyroptosis, we conducted metabolomics analysis to evaluate its impact on myeloid cell metabolism. Principal Component Analysis (PCA) was employed to compare metabolite profiles among the Con, LPS + ATP, and LPS + ATP + FG@PEV groups, revealing significant differences (Fig. S9). Notably, lipid and lipid-like molecules were found to be the predominant metabolites detected in the cells (Fig. 5A). The Venn diagram (Fig. S10) was used to observe the metabolites Con and the common differential metabolites between the LPS + ATP treatment and LPS + ATP + FG@PEV. Metabolites meeting the criteria of ($|\log FC| \geq 1$, $p < 0.05$ and VIP ≥ 1) were considered as differentially significant metabolites. A total of 740 differentially significant metabolites were identified, and their expression levels were depicted using volcano plots (Fig. 5B). A total of 8 metabolites within 3 lipid metabolic pathways were found to exhibit alterations in degenerative NPCs treated with FG@PEV, as depicted in the heatmap. The results suggest that FG@PEV may enhance the biosynthesis of unsaturated fatty acids, as well as the metabolism of fatty acids and glycerophospholipids (Fig. 5C). The results of KEGG enrichment and pathway analyses indicated that the introduction of FG@PEV had a notable impact on the metabolic pathways related to glycine, serine, and threonine, as well as protein digestion and absorption, and glutathione metabolism in myelin cells.

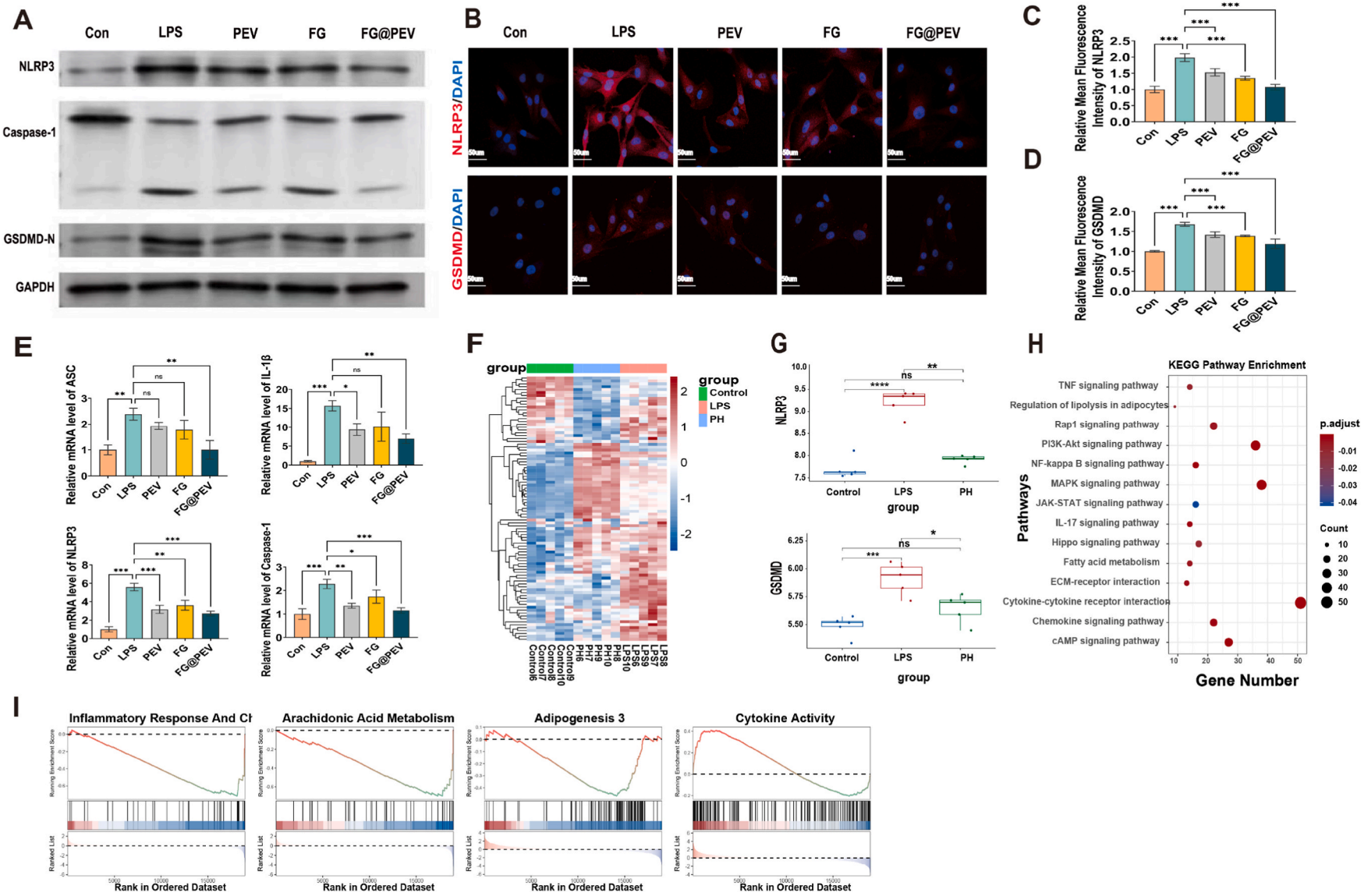

Fig. 4. FG@PEV inhibits LPS-stimulated inflammatory and pyroptosis responses in NPC. (A) Western blot analysis showing NLRP3,Caspase-1,GSDMD-N protein levels in various groups. (B) Immunofluorescence staining of NLRP3 and GSDMD in NPCs; scale bar, 50 μm; n = 5 per group. (C–D) Immunofluorescence quantification of NLRP3 and GSDMD in NPCs. (E) Quantification of pro-inflammatory marker genes (ASC, NLRP3, IL-1β, and Caspase-1) expression in NPCs by RT-PCR; n = 5 per group.(F) Heatmap showing inflammation-associated differentially expressed genes in NPCs. (G) Venn diagrams of differentially expressed genes detected in NPCs after LPS + ATP or LPS + ATP + FG@PE treatments (|log2FC|>1; p < 0.05). (H) KEGG enrichment analysis of differentially expressed genes between LPS + ATP and LPS + ATP + FG@PE groups. (I) Gene set enrichment analysis (GSEA) was applied to compare the gene sets involved in reactive oxygen metabolic processes, cytokines and inflammatory responses, fatty acid metabolism and adipocyte differentiation between LPS + ATP and LPS + ATP + FG@PE groups. (* : P < 0.05 , ** : P < 0.01 , *** : P < 0.001) .

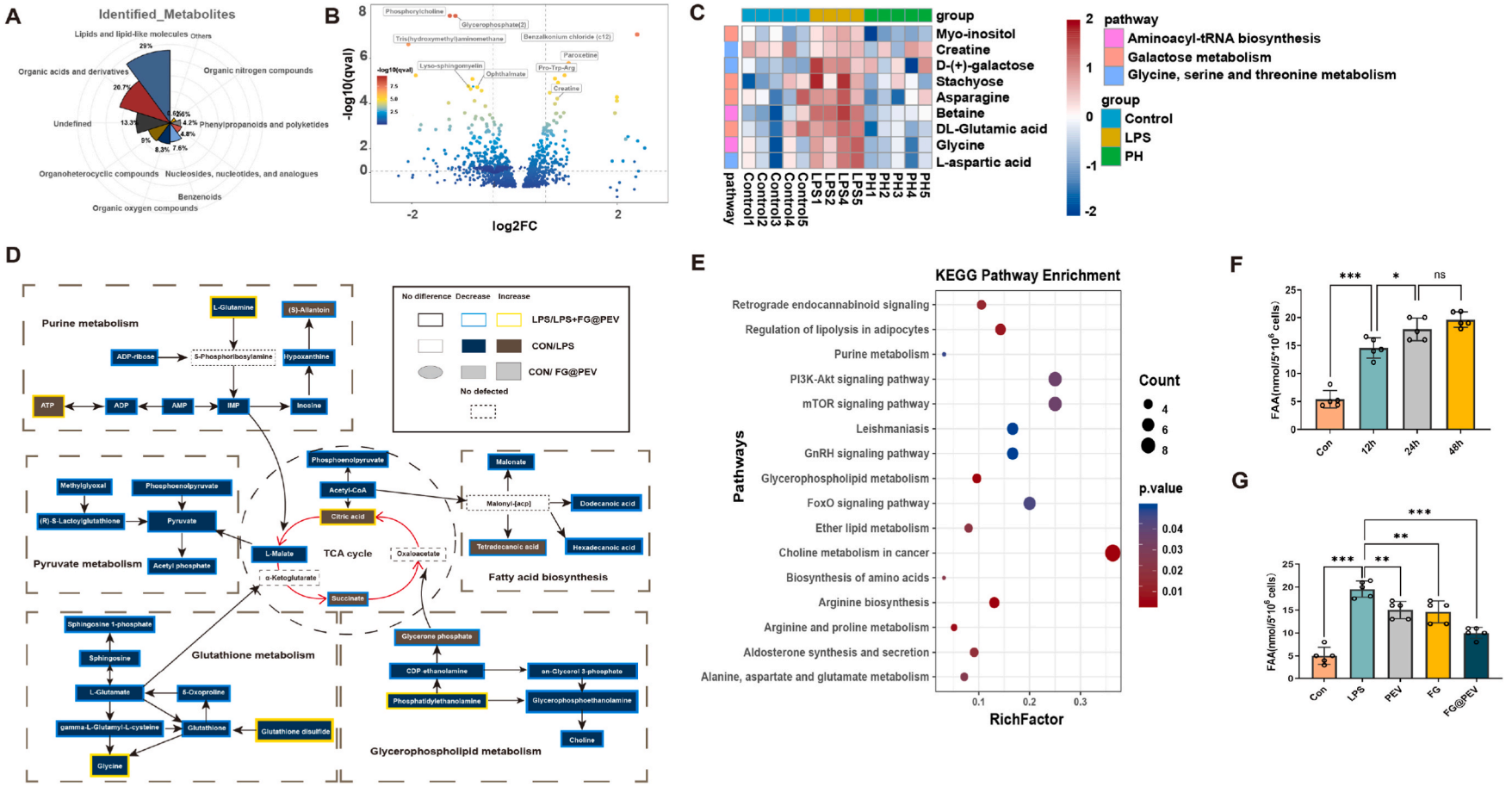

Fig. 5. FG@PEV is a key substance regulating metabolism in degenerative NPCs. (A) Non-targeted metabolites detected by metabolite molecular types (B) Volcano plots of metabolites differentially detected between the three groups (C) Heat maps of metabolites differentially detected using FDR-adjusted p-values between Con and LPS + ATP and LPS + ATP + FG@PEV. (D) Integration of transcriptomics analysis and metabolomics results of the three groups. (E) Enrichment analysis of differential metabolite sets between treatment with LPS + ATP and LPS + ATP + FG@PEV. (F) Quantitative analysis of FAA in NPs incubated for 48 h. (G) Quantitative analysis of FAA in NPs added to NPCs induced by treatment of LPS + ATP with FG, PEV, and FG@PEV, respectively, for 24 h in culture. (* : $P < 0.05$, ** : $P < 0.01$, *** : $P < 0.001$).

These findings suggest that FG@PEV exerts its influence on these diverse pathways (Fig. 5D). Next, we integrated transcriptomic and metabolomic analyses (Fig. 5E), and the results suggested that FG@PEV could promote fatty acid metabolic processes. We confirmed this by examining fatty acid metabolism, and the results showed that myeloid fatty acids (FAA) peaked after 24 h after normal culture (Fig. 5F). Stimulation of NPCs by LPS + ATP was observed under the amount of FAA produced in Con, LPS + ATP, LPS + ATP + PEV, LPS + ATP + FG, and LPS + ATP + FG@PEV, and FG@PEV reduced the accumulation of FAA. The findings indicate that FG@PEV may enhance the involvement of fatty acid metabolism in NPs, as evidenced by the increased levels of fatty acids induced by LPS + ATP stimulation (Fig. 5G).

3.6. Effect of FG@PEV on NP cell metabolis

The tissues affected by IVDD exhibit a reduction in extracellular matrix (ECM) matrix and an increased presence of degradation markers, such as matrix metalloproteinase (MMP). To investigate the impact of FG@PEV on nucleus pulposus (NP) cells, we utilized western bolt and immunofluorescence to analyze the expression of genes related to both ECM matrix synthesis and degradation. Western blot analysis confirmed that the addition of FG@PEV resulted in an enhanced protein expression level of anabolic genes (Col2, sox9, aggrecan) and a decreased protein expression level of catabolic genes (mmp3, mmp13, adamts5) in LPS-stimulated NPCs compared to cells treated with LPS + ATP (Fig. 6 A). Immunofluorescence confirmed that FG@PEV enhanced the fluorescence intensity of Col2 and MMP13 and decreased the fluorescence intensity of Col2 and MMP13 in LPS-stimulated NPCs compared with LPS group (Fig. 6B and C). Furthermore, The results of qPCR were consistent with those of western blot (Fig. 6D). In light of the available data, it can be inferred that FG@PEV exerts an inhibitory effect on the degradation of the extracellular matrix (ECM).

3.7. FG@PEV delays disc degeneration in the rat IVDD model

FG@PEV has been shown to enhance fatty acid metabolism and suppress inflammation and pyroptosis in myeloid cells. In order to ascertain the impact of FG@PEV on delaying IVDD in rats, we created a rat IVDD model by puncturing the rat tail. Initially, we employed manual palpation to confirm the appropriate caudal intervertebral plane for puncture in 8-week-old rats, followed by the injection of FG@PEV into the intervertebral disc one week later (Fig. 7 A). The intervertebral discs were excised at weeks 4 and 8 following FG@PEV injection. Subsequently, the disc heights and indices were quantified and computed from CT images (Fig. 7B). The regeneration of the nucleus pulposus (NP) was visualized using magnetic resonance imaging (MRI), and the disc's signal intensity was assessed as an indicator of high water content in the NP, based on the observation of T2-weighted signals after the 4th and 8th weeks of FG@PEV injection (Fig. 7C). The statistical analysis revealed a progressive decrease in T2-weighted signals in the IVDD group, while the FG@PEV group exhibited a lesser degree of degeneration and maintained relatively stable T2-weighted signals (Fig. 7D and E). These findings indicate that FG@PEV has the potential to delay intervertebral disc degeneration (IVDD) and restore disc structure. Furthermore, micro-computed tomography (micro-CT) and disc height index (DHI) analyses were conducted to assess disc gap height (Fig. 7F). Study findings indicate that the Control group showed no significant changes in intervertebral space height throughout the study duration. Conversely, the IVDD group exhibited intervertebral disc degeneration (IVDD) with decreased height at weeks 4 and 8. Interestingly, this trend was not evident in the FG@PEV group. Micro-CT results were consistent with MRI findings (Fig. 7G and H), implying that FG@PEV treatment could effectively maintain disc height and hinder IVDD progression. Subsequently, confirmation was sought through the utilization of H&E and S&O staining techniques, which revealed that the control group displayed typical disc tissue morphology (Fig. 7I and J). The findings demonstrated a significant restoration of intervertebral disc structure in the IVD injected with FG@PEV, as compared to the IVDD group (Fig. 7K-L). These results provide evidence that FG@PEV exhibits a notable capacity to effectively impede the progression of intervertebral disc degeneration in an in vivo setting.

3.8. FG@PEV delays cellular pyroptosis and maintains ECM matrix homeostasis

Immunofluorescence was employed to ascertain the expression of NLRP3 and GSDMD across various groups. Notably, the expression levels of NLRP3 and GSDMD were considerably elevated in the IVDD group as compared to the SHAM group (Fig. 8 A- B). However, the administration of FG@PEV treatment resulted in a significant reduction in the expression levels of NLRP3 and GSDMD when compared to the IVDD group. The data presented in this study indicate that FG@PEV has the ability to inhibit pyroptosis in myeloid cells. Intervertebral disc degeneration (IVDD) involves reduced extracellular proteoglycans and heightened expression of matrix-degrading enzymes like matrix metalloproteinases (MMPs). Our findings demonstrate that the delivery of FG@PEV leads to a decrease in MMP13 expression, while also maintaining the expression levels of COL2 (Fig. 8C and D). These results suggest that FG@PEV can effectively alleviate myeloid cell pyroptosis in vivo, thereby preserving the homeostasis of the extracellular matrix (ECM). Additionally, FG@PEV shows promising therapeutic potential in mitigating the progression of IVDD.

4. Discussion

In this study, a novel composite hydrogel was synthesized by combining fibrin and platelet extravasated vesicles, demonstrating its potential to effectively mitigate disc degeneration through the synergistic interaction of both components. In comparison to other carrier-based composite hydrogels [33–35], FG@PEV demonstrates ease of acquisition and convenience in preparation, alongside superior biological functionalities. FG can inhibit the generation of peroxides [36], synergizing with PEV to exert antioxidative effects within the intervertebral disc, thereby promoting disc repair. Additionally, FG can interact with various plasma proteins and cells to withstand biochemical and biomechanical disruptions, facilitating wound healing [37]. Firstly, FG@PEV effectively reinstates the equilibrium between ECM synthesis and catabolism by suppressing the inflammatory microenvironment within the medulla oblongata. Secondly,FG@PEV corrects disruptions in cellular fatty acid metabolism, subsequently impeding nucleus pulposus cell pyroptosis and thereby mitigating disc degeneration. Ultimately, the injection of FG@PEV into the intervertebral discs of rats was performed and subsequently validated.

The mechanical strength and ductility of fibrin hydrogel are relatively low, but the activation of anti-inflammatory cytokines by FG contributes to its anti-inflammatory effects [38,39]. The scaffolding structure formed by fibrin gel provides stable support to the wound, facilitating tissue regeneration and repair [40]. Given the limitations of the injection site, it is crucial to maintain the hydrogel in a low viscosity state, which facilitates delivery and minimizes the force and shear required for injection [41,42]. At non-optimal temperatures, the biopolymers in the hydrogel may experience a substantial increase in viscosity [43]. The study findings indicate that fibrin hydrogels possess attributes of low modulus, temperature insensitivity, and low viscosity. Furthermore, examination through scanning electron microscopy revealed the presence of large pores in FG@PEV, which facilitate nutrient exchange and create a conducive environment for cell proliferation [44]. FG@PEV demonstrates superior biocompatibility and larger pores, and the amalgamation of high biocompatibility, strong cell adhesion, and substantial porosity enables easy infiltration of cells into the hydrogel, ultimately promoting tissue regeneration [45]. PEVs have been identified as playing significant roles in hemostasis,

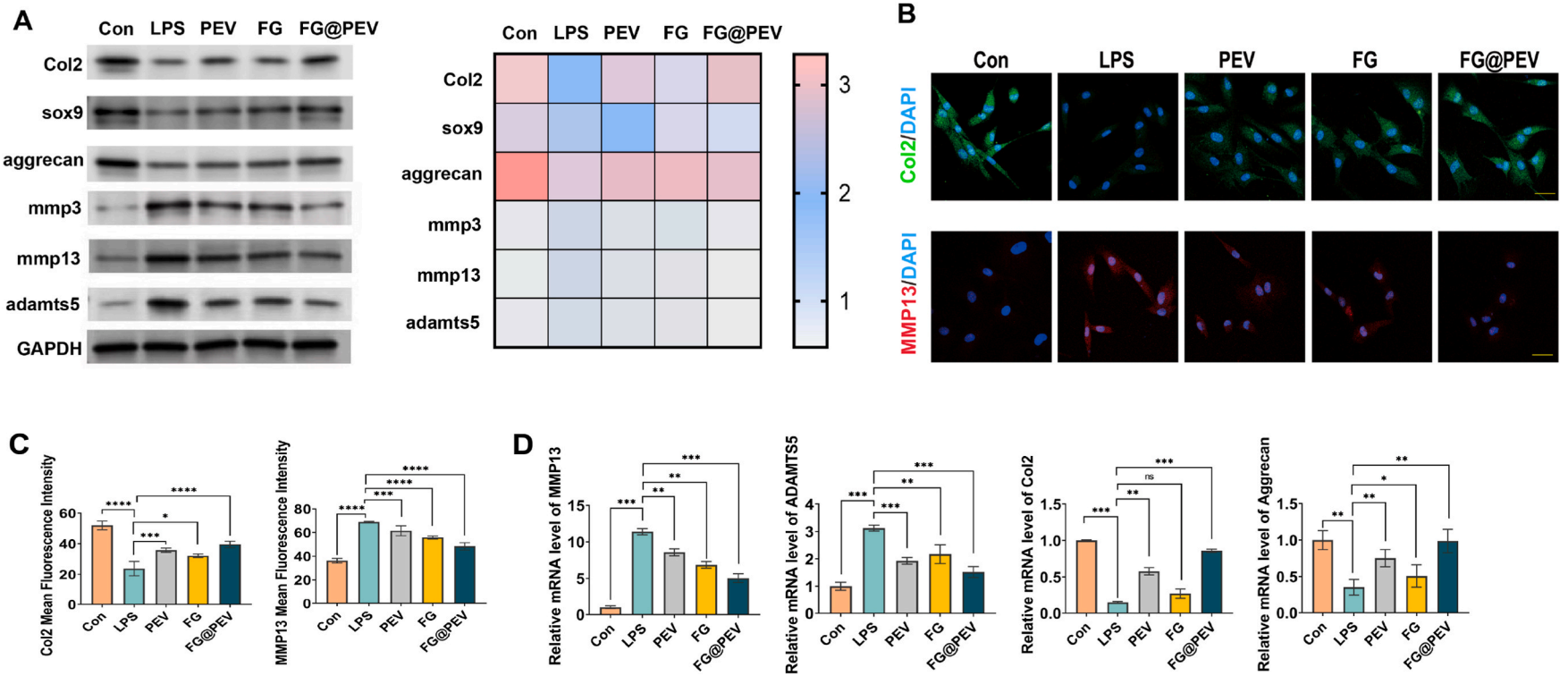

Fig. 6. Effect of FG@PEV on metabolic proteins in NPCs. (A)Western blot analysis showing Col2α, Sox9, Aggrecan, MMP3, MMP13, and ADAMTS5 protein levels in various groups. (B) Immunofluorescence assays gauged Col2 and MMP13 expression. Scale bar = 50 μm. (C) Quantified immunofluorescence intensity for Col2 and MMP13. (D) mRNA levels linked to ECM matrix synthesis and catabolism were quantified. Data are expressed as mean ± SD (n = 5). (* : $P < 0.05$, ** : $P < 0.01$, *** : $P < 0.001$) .

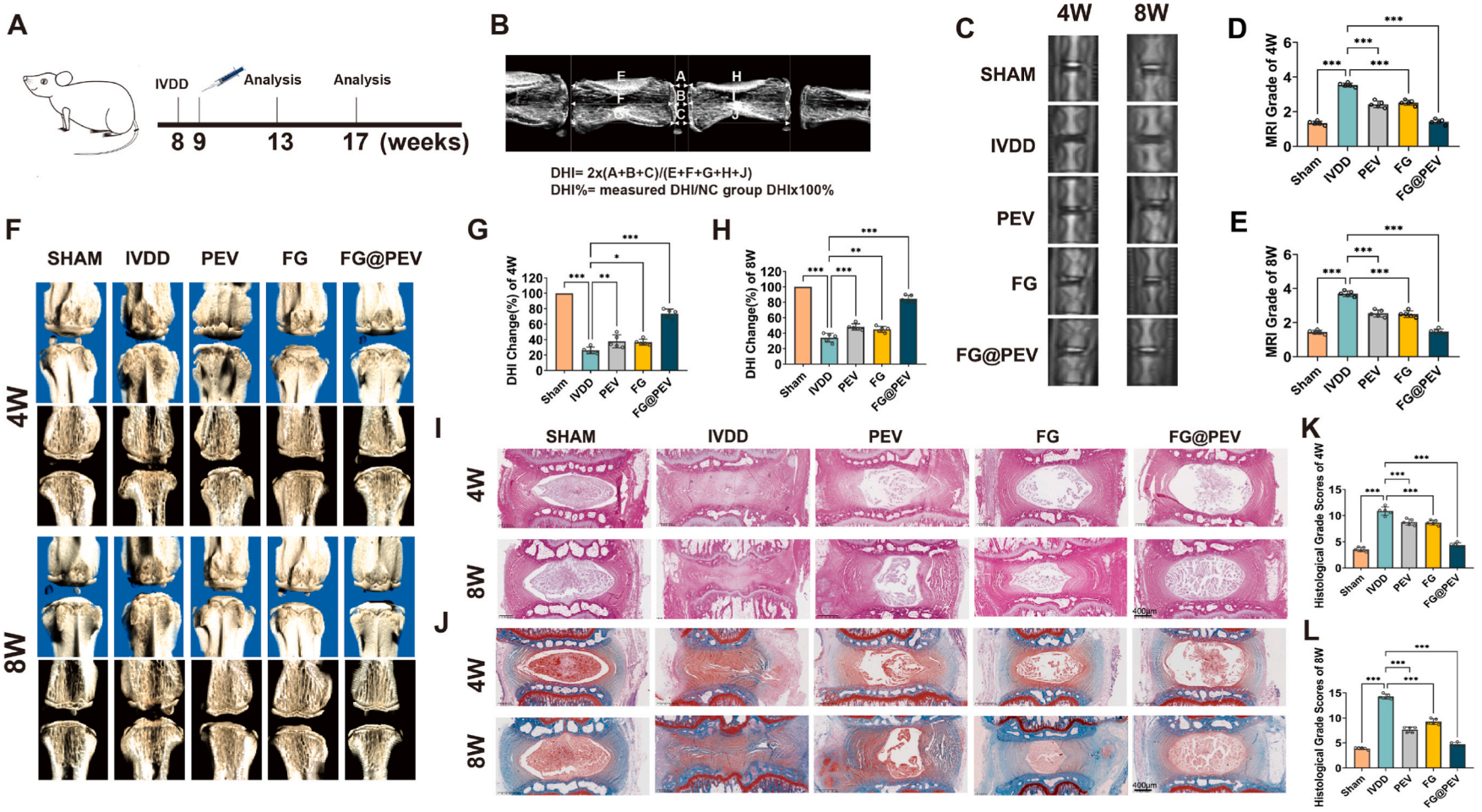

Fig. 7. FG@PEV retards disc degeneration in the rat IVDD model. (A) Overview of animal experiments in the puncture model of IVDD rats (B) Calculation formula for the measurement of disc height index in rats. (C) MRI images showing rat tailbone at 4 and 8 weeks post FG@PEV injection. (D–E) Quantitative T2-weighted signal intensity analysis of NP at 4 and 8 weeks. (F) Micro-CT images representing rat tailbone at 4 and 8 weeks. (G–H) DHI% quantification for each group. (I–J) H&E and S&O staining images of intervertebral discs at 4 and 8 weeks following FG@PEV injection. (K) Changes in histologic evaluation of H&E stained images. (L) Changes in histologic assessment of Safranin O staining images. Data are expressed as mean ± SD (n = 8).. (*: $p < 0.05$, **: $p < 0.01$, ***: $p < 0.001$.)

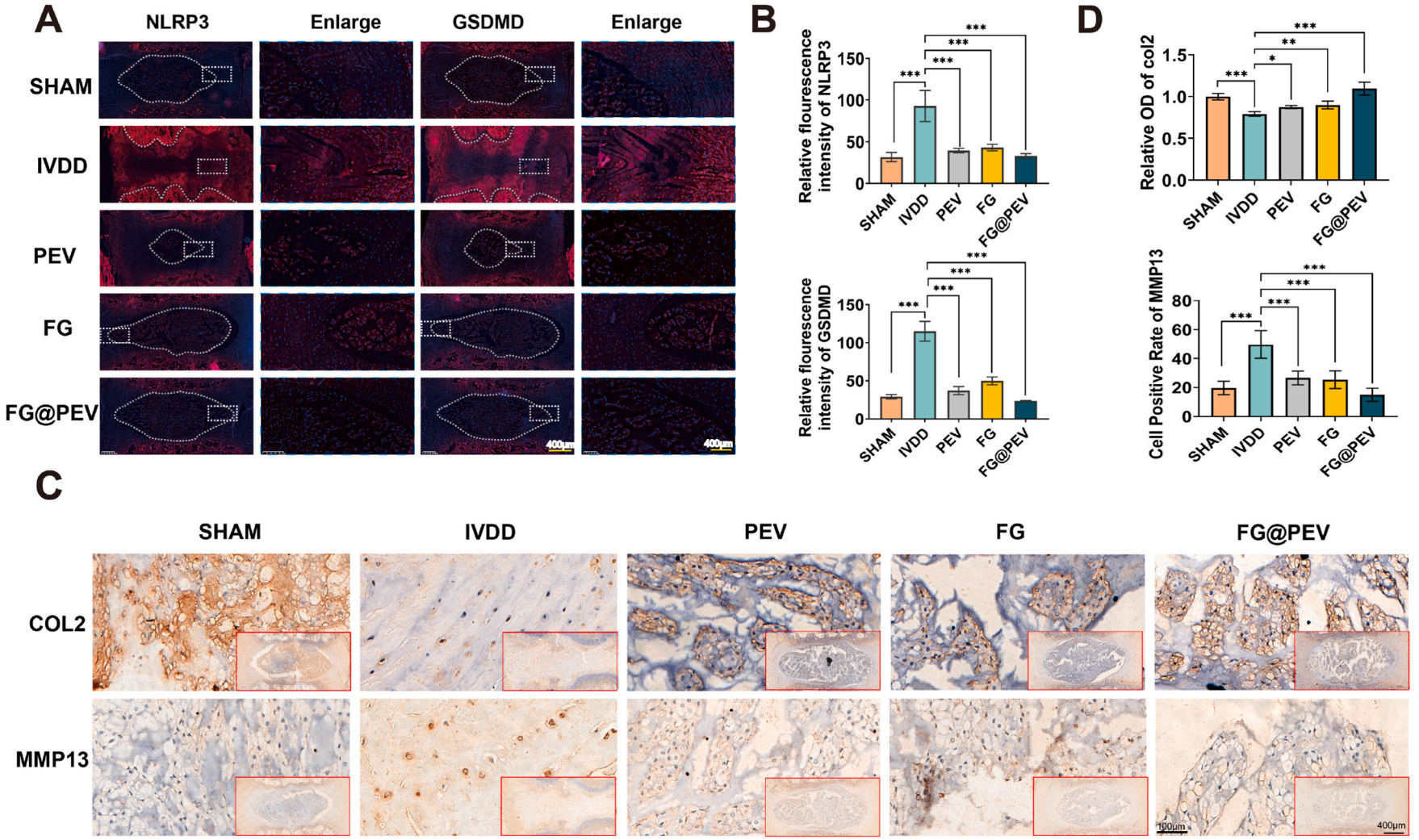

Fig. 8. Immunofluorescence and immunohistochemical histological analysis of intervertebral discs in IVDD rats. (A) Immunofluorescence method to detect the expression of NLRP3 and GSDMD in rat intervertebral disc tissues. Scale bar = 400 μm (B) The relative fluorescence intensity of NLRP3 and GSDMD was calculated from the results of immunofluorescence method. (C) Expression of COL2 and MMP13 in rat intervertebral disc tissues by immunohistochemistry. (D) The rate and relative intensity of COL2-and MMP13-positive cells were calculated from the immunohistochemical staining results. Data are expressed as mean ± SD (n = 8). (*: $p < 0.05$, **: $p < 0.01$, ***: $p < 0.001$).

immunomodulation, and pro-angiogenic processes [46]. Furthermore, multiple studies have indicated that PEVs exhibit elevated levels of growth factors, thereby showcasing their considerable potential in the realm of tissue repair and regeneration [47]. Moreover, PEVs possess a size range of 100–200 nm and possess a phospholipid bilayer structure, rendering them highly permeable across bodily tissue barriers and readily internalized by tissues or cells [48]. The actin network plays an important role in various cellular processes including endocytosis and motility [49]. By employing specific inhibitors, we obstructed a particular mechanism of endocytosis [50–52]and observed that the uptake of FG@PEV nanoparticles with a diameter of 100–120 nm by NPCs primarily occurred through actin-mediated endocytosis. Lysosomes play a pivotal role in cellular function [53]. To demonstrate that FG@PEV is not degraded within lysosomes and can escape them with the aid of delivery carriers, we utilized Cy5.5 as a model protein to visualize intracellular delivery. The findings of this study indicate that a significant proportion of FG@PEV particles have the ability to evade lysosomal degradation within NPCs. This study also provides evidence that FG@PEV particles can be shielded from lysosome-mediated degradation, allowing for the release of PEV into the cytoplasm. Furthermore, flow cytometry results demonstrate the effective inhibition of ROS production by FG@PEV hydrogel. Additionally, numerous studies have consistently demonstrated that the suppression of ROS can effectively alleviate inflammation [54], thereby promoting the therapeutic potential of FG@PEV hydrogel in the context of disc degeneration. The aforementioned findings suggest that the FG@PEV hydrogel exhibits favorable mechanical characteristics and holds significant promise for mitigating disc degeneration.

Prior research has demonstrated that the application of lipopolysaccharide (LPS) and ATP mimicry to nucleus pulposus cells can effectively replicate the inflammatory and focal conditions observed in intervertebral disc degeneration [55,56]. Our transcriptome findings align with this, as LPS and ATP stimulation induced the activation of inflammation-related pathways, namely NF-kappaβ, MAPK, and TNF, within the nucleus pulposus. Additionally, this stimulation resulted in the activation of markers associated with focal death, such as NLRP3 and GSDMD activity. Furthermore, it has been observed that the presence of LPS and adenosine triphosphate (ATP) in the inflammatory milieu induces the generation of ROS while impeding the metabolic pathways associated with fatty acids. Moreover, our investigation involving histochemical analysis of degenerated intervertebral discs has confirmed the heightened expression of NLRP3 in degenerated tissues. Hence, the effectiveness of therapeutic approaches lies in the inhibition of the inflammatory microenvironment, enhancement of metabolic function in nucleus pulposus cells, and suppression of cellular pyroptosis. Previous research has demonstrated a close association between juxtaposition and inflammatory responses, which is mediated by cysteoaspartic enzymes (such as caspase −1/-4/-5/-11) and the GSDMD family, also known as secondary necrosis [57]. Furthermore, transcriptome analysis has indicated that the FG@PEV intervention can impede the pathway linked to LPS + ATP-induced inflammation and juxtaposition of medulloblasts. Moreover, the application of FG@PEV treatment exhibited a significant reduction in the expression levels of genes associated with pyroptosis in myeloid cells, namely NLRP3, GSDMD, caspase-1, IL-1β, and IL-18. Additionally, the analysis of transcriptional enrichment indicated that FG@PEV treatment effectively stimulated the metabolic process of fatty acids in myeloid cells. It is worth noting that lipid metabolism plays a crucial role in the generation of various bioactive lipid molecules, which serve as pivotal initiators and intrinsic regulators of pyroptosis. These bioactive lipid molecules have been found to facilitate pyroptosis by disrupting the intrinsic pathways involved in the production of ROS, endoplasmic reticulum (ER) stress, mitochondrial dysfunction, lysosomal disruption, and expression of associated molecules [58]. Recent research has demonstrated that the activation of NLRP3 inflammasome can induce lipid accumulation and pyroptosis in hepatocytes through the stimulation of free fatty acids [59]. Hence, we conducted a comprehensive examination of the outcomes through metabolomics, revealing that FG@PEV intervention facilitated the breakdown of fatty acid metabolites while impeding the process of fatty acid synthesis. This finding was further substantiated by our experimental data, which indicated a reduction in fatty acid synthesis within NPCs upon the addition of FG@PEV treatment. Consequently, it can be inferred that FG@PEV possesses the potential to hinder the demise of nucleus pulposus cells by rectifying the disorder in fatty acid metabolism, thereby retarding the progression of disc degeneration.

In the in vitro evaluation, FG@PEV demonstrated the ability to impede the apoptosis of nucleus pulposus cells and retard the degeneration of intervertebral discs by upholding the homeostasis program of the ECM. The degeneration of intervertebral discs is distinguished by the degradation of proteoglycans and dehydration, resulting in diminished height of the intervertebral disc and alterations in its structure [60]. For this investigation, we employed a model of nucleus pulposus degeneration induced through intradiscal puncture [60,61]. The injection of FG@PEV hydrogel into the degenerated intervertebral disc (IVD) demonstrated its beneficial effects in restoring disc degeneration, repairing annulus fibrosus defects, and maintaining the morphology of NP tissues. The presence of inflammatory vesicles GSDMD and NLRP3 was found to be closely associated with cellular pyroptosis in the nucleus pulposus. Immunohistochemistry results indicated that FG@PEV could alleviate cellular pyroptosis in the nucleus pulposus by inhibiting the expression levels of GSDMD and NLRP3. In addition, FG@PEV can maintain the balance of ECM synthesis and catabolism by alleviating NP cell pyroptosis and delaying the degeneration of NP tissues.

5. Conclusion

In summary, we have successfully synthesized a novel hydrogel that demonstrates promising potential in mitigating disc degeneration. The hydrogel formulation involved the incorporation of platelet vesicles into a fibrin-based matrix, resulting in a hydrogel with favorable attributes such as tissue regenerative repair, biocompatibility, biodegradability, and sustained release properties. Furthermore, our FG@PEV hydrogel exhibited the ability to rectify aberrant fatty acid metabolism in myeloid cells, thereby impeding cellular pyroptosis. Additionally, this hydrogel formulation effectively suppressed inflammatory responses and upheld the homeostasis of ECM in nucleus pulposus cells.

Declarations

Ethics approval and consent to participate

This article involves experiments using animal or human specimens. The experimental protocol was developed in accordance with the ethical principles of the 'Helsinki Declaration' and received approval from the Ethics Committee of Zhejiang Chinese Medical University (No. 13185). Written informed consent was obtained from individuals or their guardians.

Consent for publication

All authors have read and approved the published version.

Availability of data and materials

No data was used for the research described in the article.

Competing interests

There are no conflicts of interest declared by the author.

Formatting of funding sources

Acknowledgements This work was financially supported by a grant from The Medical and Health Science and Technology Program of Zhejiang Province (2020KY748, 2023KY989 and 2024KY1379). Project of Zhejiang provincial plan for TCM science and technology (2022ZB238, 2023ZR111). Natural Science Foundation of Zhejiang Province (LBY24H290004 and LBY24H290005). We would like to express our special gratitude to the Laboratory of Hangzhou Hospital of Traditional Chinese Medicine, affiliated with Zhejiang Chinese Medical University, for their invaluable support and assistance throughout this study.

CRediT authorship contribution statement

Dong Wang: Writing – original draft, Formal analysis, Data curation. **Liangping Zhang:** Writing – original draft, Formal analysis, Data curation. **Du He:** Data curation. **Yujun Zhang:** Data curation. **Lan Zhao:** Writing – review & editing, Methodology. **Zhimin Miao:** Methodology. **Wei Cheng:** Methodology. **Chengyue Zhu:** Project administration. **Yinyan Shao:** Project administration. **Guofen Ge:** Project administration. **Hang Zhu:** Methodology. **HongTing Jin:** Writing – review & editing, Conceptualization. **Wei Zhang:** Conceptualization. **Hao Pan:** Funding acquisition, Conceptualization.

Declaration of competing interest

The authors declare that they have no conflicts of interest regarding the publication of this manuscript. No funding agency has influenced the content of this work.

Data availability

Data will be made available on request.

Acknowledgements

Several anonymous reviewers provided the authors with valuable comments and suggestions.

Abbreviations

ADAMTS-5	ADAM metallopeptidase with thrombospondin type 1 motif 5
ASC	Active stability control
DAPDH	Glyceraldehyde-3-Phosphate Dehydrogenase
DLS	dynamic light scattering
FAO	fatty acid beta-oxidation
GSDMD	Gasdermin-D
IL-1β	Interleukin-1 beta
IVDD	intervertebral disc degeneration
LBP	low back pain
LPS	Lipopolysaccharides
MMP3	Matrix metalloproteinase-3
NLRP3	NOD-like receptor protein 3
NP	nucleus pulposus
NOX4	NADPH oxidase 4
PLTs	platelets
PEVs	platelet-derived extracellular vesicles
ROS	reactive oxygen species
SEM	the scanning electron microscopy

Appendix A. Supplementary data

Supplementary data to this article can be found online at https://doi.org/10.1016/j.mtbio.2024.101081.

References

[1] P. Cazzanelli, K. Wuertz-Kozak, MicroRNAs in intervertebral disc degeneration, apoptosis, inflammation, and mechanobiology, Int. J. Mol. Sci. 21 (10) (2020).
[2] J. Hartvigsen, M.J. Hancock, A. Kongsted, Q. Louw, M.L. Ferreira, S. Genevay, et al., What low back pain is and why we need to pay attention, Lancet 391 (10137) (2018) 2356–2367.
[3] S. Chen, M. Chen, X. Wu, S. Lin, C. Tao, H. Cao, et al., Global, regional and national burden of low back pain 1990-2019: a systematic analysis of the Global Burden of Disease study 2019, J Orthop Translat 32 (2022) 49–58.
[4] B.G. Peng, Pathophysiology, diagnosis, and treatment of discogenic low back pain, World J. Orthoped. 4 (2) (2013) 42–52.
[5] S. Zhang, B. Hu, W. Liu, P. Wang, X. Lv, S. Chen, et al., The role of structure and function changes of sensory nervous system in intervertebral disc-related low back pain, Osteoarthritis Cartilage 29 (1) (2021) 17–27.
[6] Y. Wang, M. Che, J. Xin, Z. Zheng, J. Li, S. Zhang, The role of IL-1beta and TNF-alpha in intervertebral disc degeneration, Biomed. Pharmacother. 131 (2020) 110660.
[7] E.S. Silagi, I.M. Shapiro, M.V. Risbud, Glycosaminoglycan synthesis in the nucleus pulposus: dysregulation and the pathogenesis of disc degeneration, Matrix Biol. 71–72 (2018) 368–379.
[8] A. Dimozi, E. Mavrogonatou, A. Sklirou, D. Kletsas, Oxidative stress inhibits the proliferation, induces premature senescence and promotes a catabolic phenotype in human nucleus pulposus intervertebral disc cells, Eur. Cell. Mater. 30 (2015) 89–102, discussion 3.
[9] W. Zhang, G. Li, R. Luo, J. Lei, Y. Song, B. Wang, et al., Cytosolic escape of mitochondrial DNA triggers cGAS-STING-NLRP3 axis-dependent nucleus pulposus cell pyroptosis, Exp. Mol. Med. 54 (2) (2022) 129–142.
[10] K. Zhao, R. An, Q. Xiang, G. Li, K. Wang, Y. Song, et al., Acid-sensing ion channels regulate nucleus pulposus cell inflammation and pyroptosis via the NLRP3 inflammasome in intervertebral disc degeneration, Cell Prolif. 54 (1) (2021) e12941.
[11] J. Ding, K. Wang, W. Liu, Y. She, Q. Sun, J. Shi, et al., Pore-forming activity and structural autoinhibition of the gasdermin family, Nature 535 (7610) (2016) 111–116.
[12] J.S. Moon, K. Nakahira, K.P. Chung, G.M. DeNicola, M.J. Koo, M.A. Pabon, et al., NOX4-dependent fatty acid oxidation promotes NLRP3 inflammasome activation in macrophages, Nat. Med. 22 (9) (2016) 1002–1012.
[13] F. Puhm, E. Boilard, K.R. Machlus, Platelet extracellular vesicles: beyond the blood, Arterioscler. Thromb. Vasc. Biol. 41 (1) (2021) 87–96.
[14] A. Ceroi, F.A. Delettre, C. Marotel, T. Gauthier, A. Asgarova, S. Biichle, et al., The anti-inflammatory effects of platelet-derived microparticles in human plasmacytoid dendritic cells involve liver X receptor activation, Haematologica 101 (3) (2016) e72–e76.
[15] S. Sadallah, C. Eken, P.J. Martin, J.A. Schifferli, Microparticles (ectosomes) shed by stored human platelets downregulate macrophages and modify the development of dendritic cells, J. Immunol. 186 (11) (2011) 6543–6552.
[16] M. Antich-Rossello, M.A. Forteza-Genestra, M. Monjo, J.M. Ramis, Platelet-derived extracellular vesicles for regenerative medicine, Int. J. Mol. Sci. 22 (16) (2021).
[17] L.C. Edelstein, The role of platelet microvesicles in intercellular communication, Platelets 28 (3) (2017) 222–227.
[18] Z. Dai, C. Xia, T. Zhao, H. Wang, H. Tian, O. Xu, et al., Platelet-derived extracellular vesicles ameliorate intervertebral disc degeneration by alleviating mitochondrial dysfunction, Mater Today Bio 18 (2023) 100512.
[19] Z.L. Hu, H.Y. Li, X. Chang, Y.Y. Li, C.H. Liu, X.X. Gao, et al., Exosomes derived from stem cells as an emerging therapeutic strategy for intervertebral disc degeneration, World J. Stem Cell. 12 (8) (2020) 803–813.
[20] H. Xing, Z. Zhang, Q. Mao, C. Wang, Y. Zhou, X. Zhou, et al., Injectable exosome-functionalized extracellular matrix hydrogel for metabolism balance and pyroptosis regulation in intervertebral disc degeneration, J. Nanobiotechnol. 19 (1) (2021) 264.
[21] S. Liberski, M. Wichrowska, J. Kociecki, Aflibercept versus faricimab in the treatment of neovascular age-related macular degeneration and diabetic macular edema: a review, Int. J. Mol. Sci. 23 (16) (2022).
[22] B.P. Antunes, M.L. Vainieri, M. Alini, E. Monsonego-Ornan, S. Grad, A. Yayon, Enhanced chondrogenic phenotype of primary bovine articular chondrocytes in Fibrin-Hyaluronan hydrogel by multi-axial mechanical loading and FGF18, Acta Biomater. 105 (2020) 170–179.
[23] C.J. Panebianco, T.J. DiStefano, B. Mui, W.W. Hom, J.C. Iatridis, Crosslinker concentration controls TGFbeta-3 release and annulus fibrosus cell apoptosis in genipin-crosslinked fibrin hydrogels, Eur. Cell. Mater. 39 (2020) 211–226.
[24] C.H.B. Reis, D.V. Buchaim, A.C. Ortiz, S.O.M. Fideles, J.A. Dias, M.A. Miglino, et al., Application of fibrin associated with photobiomodulation as a promising strategy to improve regeneration in tissue engineering: a systematic review, Polymers 14 (15) (2022).
[25] J. Zhou, Y. Liu, X. Liu, J. Wan, S. Zuo, T. Pan, et al., Hyaluronic acid-based dual network hydrogel with sustained release of platelet-rich plasma as a diabetic wound dressing, Carbohydr. Polym. 314 (2023) 120924.
[26] F. Mirjalili, M. Mahmoodi, Controlled release of protein from gelatin/chitosan hydrogel containing platelet-rich fibrin encapsulated in chitosan nanoparticles for accelerated wound healing in an animal model, Int. J. Biol. Macromol. 225 (2023) 588–604.
[27] J.P. Luyendyk, J.G. Schoenecker, M.J. Flick, The multifaceted role of fibrinogen in tissue injury and inflammation, Blood 133 (6) (2019) 511–520.

[28] X. Cheng, L. Zhang, K. Zhang, G. Zhang, Y. Hu, X. Sun, et al., Circular RNA VMA21 protects against intervertebral disc degeneration through targeting miR-200c and X linked inhibitor-of-apoptosis protein, Ann. Rheum. Dis. 77 (5) (2018) 770–779.
[29] Y. Wang, Y. Wu, B. Zhang, C. Zheng, C. Hu, C. Guo, et al., Repair of degenerative nucleus pulposus by polyphenol nanosphere-encapsulated hydrogel gene delivery system, Biomaterials 298 (2023) 122132.
[30] K. Masuda, Y. Aota, C. Muehleman, Y. Imai, M. Okuma, E.J. Thonar, et al., A novel rabbit model of mild, reproducible disc degeneration by an anulus needle puncture: correlation between the degree of disc injury and radiological and histological appearances of disc degeneration, Spine 30 (1) (2005) 5–14.
[31] C.W. Smith, Release of α-granule contents during platelet activation, Platelets 33 (2022) 491–502, https://doi.org/10.1080/09537104.2021.1913576.
[32] A.S. Weyrich, G.A. Zimmerman, Platelets: signaling cells in the immune continuum, Trends Immunol. 25 (2004) 489–495, https://doi.org/10.1016/j.it.2004.07.003.
[33] J.A. Kim, Y.H. An, H.G. Yim, W.J. Han, Y.B. Park, H.J. Park, et al., Injectable fibrin/polyethylene oxide semi-IPN hydrogel for a segmental meniscal defect regeneration, Am. J. Sports Med. 49 (6) (2021) 1538–1550.
[34] B. Nazari, M. Kazemi, A. Kamyab, B. Nazari, S. Ebrahimi-Barough, M. Hadjighassem, et al., Fibrin hydrogel as a scaffold for differentiation of induced pluripotent stem cells into oligodendrocytes, J. Biomed. Mater. Res. B Appl. Biomater. 108 (1) (2020) 192–200.
[35] C. Xia, Z. Zeng, B. Fang, M. Tao, C. Gu, L. Zheng, et al., Mesenchymal stem cell-derived exosomes ameliorate intervertebral disc degeneration via anti-oxidant and anti-inflammatory effects, Free Radic. Biol. Med. 143 (2019) 1–15.
[36] I.V. Kaplan, M. Attaelmannan, S.S. Levinson, Fibrinogen is an antioxidant that protects β-lipoproteins at physiological concentrations in a cell free system, Atherosclerosis 158 (2001) 455–463, https://doi.org/10.1016/S0021-9150(01)00452-X.
[37] A.S. Wolberg, Fibrinogen and fibrin: synthesis, structure, and function in health and disease, J. Thromb. Haemostasis 21 (2023) 3005–3015, https://doi.org/10.1016/j.jtha.2023.08.014.
[38] H.J. Kang, N. Ko, S.J. Oh, S.Y. An, Y.S. Hwang, S.Y. Kim, Injectable human hair keratin-fibrinogen hydrogels for engineering 3D microenvironments to accelerate oral tissue regeneration, Int. J. Mol. Sci. 22 (24) (2021).
[39] J.Y. Hsieh, T.D. Smith, V.S. Meli, T.N. Tran, E.L. Botvinick, W.F. Liu, Differential regulation of macrophage inflammatory activation by fibrin and fibrinogen, Acta Biomater. 47 (2017) 14–24.
[40] X. He, L. Yang, K. Dong, F. Zhang, Y. Liu, B. Ma, et al., Biocompatible exosome-modified fibrin gel accelerates the recovery of spinal cord injury by VGF-mediated oligodendrogenesis, J. Nanobiotechnol. 20 (1) (2022) 360.
[41] J.M. Alonso, J. Andrade Del Olmo, R. Perez Gonzalez, V. Saez-Martinez, Injectable hydrogels: from laboratory to industrialization, Polymers 13 (4) (2021).
[42] J.H. Lee, Injectable hydrogels delivering therapeutic agents for disease treatment and tissue engineering, Biomater. Res. 22 (2018) 27.
[43] A.B. Bello, D. Kim, D. Kim, H. Park, S.H. Lee, Engineering and functionalization of gelatin biomaterials: from cell culture to medical applications, Tissue Eng Part B Rev 26 (2) (2020) 164–180.
[44] N. Annabi, J.W. Nichol, X. Zhong, C. Ji, S. Koshy, A. Khademhosseini, et al., Controlling the porosity and microarchitecture of hydrogels for tissue engineering, Tissue Eng Part B Rev 16 (4) (2010) 371–383.
[45] J. Luo, A. Darai, T. Pongkulapa, B. Conley, L. Yang, I. Han, et al., Injectable bioorthogonal hydrogel (BIOGEL) accelerates tissue regeneration in degenerated intervertebral discs, Bioact. Mater. 23 (2023) 551–562.
[46] A.T. Franco, A. Corken, J. Ware, Platelets at the interface of thrombosis, inflammation, and cancer, Blood 126 (5) (2015) 582–588.
[47] E. Torreggiani, F. Perut, L. Roncuzzi, N. Zini, S.R. Baglio, N. Baldini, Exosomes: novel effectors of human platelet lysate activity, Eur. Cell. Mater. 28 (2014) 137–151, discussion 51.
[48] J. Wu, Y. Piao, Q. Liu, X. Yang, Platelet-rich plasma-derived extracellular vesicles: a superior alternative in regenerative medicine? Cell Prolif. 54 (12) (2021) e13123.
[49] J. Chung, B.L. Goode, J. Gelles, Single-molecule analysis of actin filament debranching by cofilin and GMF, Proc. Natl. Acad. Sci. U.S.A. 119 (29) (2022) e2115129119.
[50] V. Bandmann, J.D. Muller, T. Kohler, U. Homann, Uptake of fluorescent nano beads into BY2-cells involves clathrin-dependent and clathrin-independent endocytosis, FEBS Lett. 586 (20) (2012) 3626–3632.
[51] K. Sato, J. Nagai, N. Mitsui, Y. Ryoko, M. Takano, Effects of endocytosis inhibitors on internalization of human IgG by Caco-2 human intestinal epithelial cells, Life Sci. 85 (23–26) (2009) 800–807.
[52] W.L. Schulz, A.K. Haj, L.A. Schiff, Reovirus uses multiple endocytic pathways for cell entry, J. Virol. 86 (23) (2012) 12665–12675.
[53] T. Zhang, X.Q. Hong, H.T. Zhi, J. Hu, W.H. Chen, Synthesis and mechanism of biological action of morpholinyl-bearing arylsquaramides as small-molecule lysosomal pH modulators, RSC Adv. 12 (35) (2022) 22748–22759.
[54] M. Meng, R. Huo, Y. Wang, N. Ma, X. Shi, X. Shen, et al., Lentinan inhibits oxidative stress and alleviates LPS-induced inflammation and apoptosis of BMECs by activating the Nrf2 signaling pathway, Int. J. Biol. Macromol. 222 (Pt B) (2022) 2375–2391.
[55] T. Ohnishi, N. Iwasaki, H. Sudo, Causes of and molecular targets for the treatment of intervertebral disc degeneration: a review, Cells 11 (3) (2022).
[56] R. Shen, P. Yin, H. Yao, L. Chen, X. Chang, H. Li, et al., Punicalin ameliorates cell pyroptosis induced by LPS/ATP through suppression of ROS/NLRP3 pathway, J. Inflamm. Res. 14 (2021) 711–718.
[57] M.T. Silva, Bacteria-induced phagocyte secondary necrosis as a pathogenicity mechanism, J. Leukoc. Biol. 88 (5) (2010) 885–896.
[58] Y. Qiu, Y.N. Shi, N. Zhu, S. Zhang, C.J. Zhang, J. Gu, et al., A lipid perspective on regulated pyroptosis, Int. J. Biol. Sci. 19 (8) (2023) 2333–2348.
[59] Q. Yao, J. Liu, Q. Cui, T. Jiang, X. Xie, X. Du, et al., CCN1/Integrin alpha(5)beta(1) instigates free fatty acid-induced hepatocyte lipid accumulation and pyroptosis through NLRP3 inflammasome activation, Nutrients 14 (18) (2022).
[60] N.V. Vo, R.A. Hartman, P.R. Patil, M.V. Risbud, D. Kletsas, J.C. Iatridis, et al., Molecular mechanisms of biological aging in intervertebral discs, J. Orthop. Res. 34 (8) (2016) 1289–1306.
[61] J. Lin, X. Zheng, Z. Zhang, J. Zhuge, Z. Shao, C. Huang, et al., Inhibition of LRRK2 restores parkin-mediated mitophagy and attenuates intervertebral disc degeneration, Osteoarthritis Cartilage 29 (4) (2021) 579–591.